

A Framework for Two-Particle Correlations with Small Centrality Binning in  
*Au + Au* Collisions Using PHENIX & Tools for Relative Calorimeter Calibrations  
Studies for sPHENIX

A thesis presented to  
the faculty of  
the College of Arts and Sciences of Ohio University

In partial fulfillment  
of the requirements for the degree  
Master of Science

Justin W. Bryan  
August 2021  
©2021 Justin W. Bryan. All Rights Reserved.

This thesis titled  
A Framework for Two-Particle Correlations with Small Centrality Binning in  
*Au + Au* Collisions Using PHENIX & Tools for Relative Calorimeter Calibrations  
Studies for sPHENIX

by  
JUSTIN W. BRYAN

has been approved for  
the Department of Physics and Astronomy  
and the College of Arts and Sciences by

Dr. Justin Frantz  
Associate Professor of Physics and Astronomy

Florentz Plassmann  
Dean, College of Arts and Sciences

# Abstract

BRYAN, JUSTIN W., M.S., August 2021, Physics & Astronomy

---

A Framework for Two-Particle Correlations with Small Centrality Binning in  $Au + Au$   
 Collisions Using PHENIX & Tools for Relative Calorimeter Calibrations Studies for  
sPHENIX

---

Director of Thesis: Justin Frantz

Accelerating nuclei to near the speed of light and smashing them together in what is known as a particle accelerator can achieve extremely high energy densities. The energy density is so large that the most fundamental particles such as quarks and gluons become a soup, or small fireball, known as the quark-gluon plasma, a state of matter found at the Relativistic Heavy Ion Collider in the year 2000 with the PHENIX experiment.

In this thesis we study two-particle correlations with  $\pi^0$ 's and charged hadrons along with their detection and calibration in calorimeter detectors. The studies represent a foundation to build towards the ultimate goal to study the effects the quark-gluon plasma has on hadronic jets that emanate from the plasma. Jet functions are then derived that can be used to show the suppression of away-side jet production, a key observable of the plasma. We study the systematics and statistical potential of two PHENIX datasets in higher centrality classes, which range from 40% to 90%, with data from Run14 and Run16. These studies include use of the double ratio ( $R_I$ ), which is a near-to-away-side yield ratio used to study suppression. Later we introduce, develop, and study techniques for calibrating three new calorimeters that are part of the upgraded sPHENIX experiment. This includes a suite of tools developed as part of the thesis that include simple and complex Monte Carlo simulations. The use of the tools are demonstrated through studies of the needed statistics and exploration of the systematics associated with performing a relative tower calibration.

## Acknowledgements

I must thank Dr. Justin Frantz for his guidance and the tremendous amount of knowledge he has given me throughout this project. I would also like to thank my committee members Dr. Hla, and Dr. Prakash for their time. I want to express sincere gratitude toward classmates and professors that have helped me throughout my studies.

## Table of Contents

|                                                                                                                                                                                              | Page      |
|----------------------------------------------------------------------------------------------------------------------------------------------------------------------------------------------|-----------|
| <b>Abstract</b> . . . . .                                                                                                                                                                    | <b>3</b>  |
| <b>Acknowledgements</b> . . . . .                                                                                                                                                            | <b>4</b>  |
| <b>List of Tables</b> . . . . .                                                                                                                                                              | <b>8</b>  |
| <b>List of Figures</b> . . . . .                                                                                                                                                             | <b>12</b> |
| <b>1 Introductions</b> . . . . .                                                                                                                                                             | <b>13</b> |
| 1.1 Fundamental Forces . . . . .                                                                                                                                                             | 14        |
| 1.1.1 Strong Nuclear Force . . . . .                                                                                                                                                         | 14        |
| 1.2 Relativistic Hardon Collisions . . . . .                                                                                                                                                 | 15        |
| 1.2.1 Event Evolution . . . . .                                                                                                                                                              | 15        |
| 1.2.2 Centrality . . . . .                                                                                                                                                                   | 16        |
| 1.2.3 Coordinate System . . . . .                                                                                                                                                            | 17        |
| 1.3 Quark-Gluon Plasma . . . . .                                                                                                                                                             | 18        |
| 1.3.1 Flow . . . . .                                                                                                                                                                         | 19        |
| 1.3.2 Jet Quenching . . . . .                                                                                                                                                                | 20        |
| 1.3.2.1 $R_{AA}$ Single Particle Suppression . . . . .                                                                                                                                       | 20        |
| 1.3.2.2 Two-particle Correlation . . . . .                                                                                                                                                   | 21        |
| 1.4 Motivation of Thesis . . . . .                                                                                                                                                           | 22        |
| <b>2 Experimental Details</b> . . . . .                                                                                                                                                      | <b>24</b> |
| 2.1 Introduction . . . . .                                                                                                                                                                   | 24        |
| 2.2 Relativistic Heavy Ion Collider . . . . .                                                                                                                                                | 24        |
| 2.3 PHENIX . . . . .                                                                                                                                                                         | 25        |
| 2.3.1 Global Detectors . . . . .                                                                                                                                                             | 27        |
| 2.3.1.1 Beam-Beam Counter & Zero Degree Calorimeter . . . . .                                                                                                                                | 27        |
| 2.3.2 Central Arm Detectors . . . . .                                                                                                                                                        | 29        |
| 2.3.2.1 Drift Chamber . . . . .                                                                                                                                                              | 29        |
| 2.3.2.2 Ring Imaging Cherenkov Detector . . . . .                                                                                                                                            | 30        |
| 2.3.2.3 Electromagnetic Calorimeter . . . . .                                                                                                                                                | 31        |
| 2.4 sPHENIX . . . . .                                                                                                                                                                        | 34        |
| 2.4.1 Electromagnetic Calorimeter . . . . .                                                                                                                                                  | 35        |
| 2.4.2 Hadronic Calorimeter . . . . .                                                                                                                                                         | 36        |
| <b>3 Part I: Development of PHENIX Framework for Studying Two-Particle Correlations and <math>R_I</math> Suppression in Small Centrality Bin Sizes and Small Collision Overlap</b> . . . . . | <b>39</b> |
| 3.1 Introduction . . . . .                                                                                                                                                                   | 39        |
| 3.2 Run Selection . . . . .                                                                                                                                                                  | 39        |
| 3.3 Particle Selection . . . . .                                                                                                                                                             | 40        |
| 3.3.1 $\pi^0$ Trigger . . . . .                                                                                                                                                              | 40        |

|       |                                                                                                                                                     |    |
|-------|-----------------------------------------------------------------------------------------------------------------------------------------------------|----|
| 3.3.2 | Photon Selection . . . . .                                                                                                                          | 41 |
| 3.3.3 | Charged Hadron Selection . . . . .                                                                                                                  | 41 |
| 3.4   | $p_T$ and Centrality Selection . . . . .                                                                                                            | 42 |
| 3.5   | Two-Particle Correlation . . . . .                                                                                                                  | 43 |
| 3.5.1 | Background and Jet Function . . . . .                                                                                                               | 44 |
| 3.6   | Double Ratio $R_I$ . . . . .                                                                                                                        | 45 |
| 3.6.1 | Bleeding Correction . . . . .                                                                                                                       | 46 |
| 4     | <b>Results for Part I: Studies of Systematics and Statistical Precision of Two-particle Correlations and <math>R_I</math> Suppression</b> . . . . . | 48 |
| 4.1   | Baseline Measurement: $p + p$ . . . . .                                                                                                             | 48 |
| 4.1.1 | Correlation & Jet Function . . . . .                                                                                                                | 48 |
| 4.2   | Run14 Minimum Bias . . . . .                                                                                                                        | 50 |
| 4.2.1 | Correlation and Jet Function . . . . .                                                                                                              | 50 |
| 4.2.2 | Hot Tower Maps . . . . .                                                                                                                            | 52 |
| 4.2.3 | Double Ratio ( $R_I$ ) . . . . .                                                                                                                    | 53 |
| 4.3   | Run16 Minimum Bias . . . . .                                                                                                                        | 56 |
| 4.3.1 | Correlation and Jet Function and Hot Tower Maps . . . . .                                                                                           | 57 |
| 4.3.2 | Double Ratio $R_I$ . . . . .                                                                                                                        | 59 |
| 5     | <b>Part II: Tools and Studies for Relative Calorimeter Calibrations in sPHENIX</b> . . . . .                                                        | 62 |
| 5.1   | Introductory Information . . . . .                                                                                                                  | 63 |
| 5.2   | Calorimeter Calibration . . . . .                                                                                                                   | 63 |
| 5.3   | HIJING and PYTHIA . . . . .                                                                                                                         | 65 |
| 5.4   | Energy Distributions . . . . .                                                                                                                      | 66 |
| 5.5   | Energy Shifts . . . . .                                                                                                                             | 68 |
| 5.6   | Monte Carlo Simulation And Alternate Functional Forms . . . . .                                                                                     | 68 |
| 6     | <b>Results for Part II: Simple MC Studies, Fitting PYTHIA Distributions, and Estimation of Required Number of Events for Calibration</b> . . . . .  | 70 |
| 6.1   | Simple Monte Carlo and Associated Studies . . . . .                                                                                                 | 70 |
| 6.1.1 | Simple MC: True Exponential Distribution . . . . .                                                                                                  | 70 |
| 6.1.2 | Simple MC: RHIC Distribution . . . . .                                                                                                              | 72 |
| 6.2   | HIJING Studies: IHCal . . . . .                                                                                                                     | 74 |
| 6.2.1 | PYTHIA IHCal Energy Shift . . . . .                                                                                                                 | 77 |
| 6.3   | PYTHIA Studies: OHCal . . . . .                                                                                                                     | 78 |
| 6.3.1 | PYTHIA OHCal Energy Shifts . . . . .                                                                                                                | 80 |
| 6.4   | PYTHIA Study: EMCAL . . . . .                                                                                                                       | 80 |
| 6.4.1 | PYTHIA EMCAL Energy Shift . . . . .                                                                                                                 | 82 |
| 6.5   | Discussion . . . . .                                                                                                                                | 83 |
| 7     | <b>Summary &amp; Outlook</b> . . . . .                                                                                                              | 85 |

|                      |    |
|----------------------|----|
| References . . . . . | 90 |
|----------------------|----|

## List of Tables

|     |                                                                                                                                          |    |
|-----|------------------------------------------------------------------------------------------------------------------------------------------|----|
| 1.1 | A summary of the four forces and their respective theory, particle mediator, and range of the force. . . . .                             | 14 |
| 1.2 | The six types of quarks and their respective charge and mass. . . . .                                                                    | 15 |
| 2.1 | A condensed description of PHENIX detectors and their spatial coverage relevant to this thesis. This table is adapted from [13]. . . . . | 26 |
| 3.1 | Year 2014 and 2016 runs with beam information and the number of events sampled over. . . . .                                             | 40 |

## List of Figures

|     |                                                                                                                                                                                                                                                                                                                                                                                         |    |
|-----|-----------------------------------------------------------------------------------------------------------------------------------------------------------------------------------------------------------------------------------------------------------------------------------------------------------------------------------------------------------------------------------------|----|
| 1.1 | Quarks (purple) are the building blocks of hadrons that appear in six flavors. Leptons (green) are half-integer spin particles (fermions), that may be charged like that of the electron or neutral like that of a neutrino or neutron. Bosons are force mediators, and the Higgs boson is how fermionic matter is given mass. Image taken from [1]. . . . .                            | 13 |
| 1.2 | The leftmost panel shows two flattened gold nuclei about to collide. The left-center panel shows the initial collision. The right-center panel now shows freed partons. The rightmost panel shows the formation of the quark-gluon plasma. Image taken from [3]. . . . .                                                                                                                | 16 |
| 1.3 | A cartoon plot of centrality classes along with other signatures of centrality classes such as number of participating particles, $\langle N_{part} \rangle$ , charged particle multiplicity $\langle N_{ch} \rangle$ , and impact parameter, $b$ . Image taken from [4]. . . . .                                                                                                       | 17 |
| 1.4 | Cartoon drawing of the coordinate system used in this study, and common among accelerator physics. $\eta$ can extend from $-\infty$ to $+\infty$ . This study sees the pseudorapidity extend from -1.1 to 1.1. . . . .                                                                                                                                                                  | 18 |
| 1.5 | A cartoon drawing of two-particles colliding (blue), and the quark-gluon plasma (orange) undergoing flow. The reaction plane is the green grid. Image taken from [6]. . . . .                                                                                                                                                                                                           | 19 |
| 1.6 | A PHENIX plot of $R_{AA}$ as a function of $p_T$ . Many different particles are plotted, but most importantly are the $\pi^0$ 's as they are the trigger in this study. Image taken from [8]. . . . .                                                                                                                                                                                   | 21 |
| 1.7 | Two-particle correlation plot from the STAR collaboration of $p + p$ (black), $d + Au$ (red), and $Au + Au$ (blue). Trigger particles with $4 < p_T^{trig} < 6$ GeV/c, and partner particles with $2 < p_T^{assoc} < p_T^{trig}$ GeV/c. Notice the away-side jet suppression for gold at the value of $\pi$ , it is indicative of the quark-gluon plasma. Image taken from [9]. . . . . | 22 |
| 2.1 | An ariel view of the RHIC complex at BNL. The yellow and dark blue lines represent the beam lines. STAR and PHENIX are experiments set up along the beam line, and other labels are smaller accelerators that eventually lead to the large beamlines. Image taken from [10]. . . . .                                                                                                    | 25 |
| 2.2 | PHENIX's Run16 detector configuration as viewed from the beam (top), and from the side (bottom). Image taken from [12]. . . . .                                                                                                                                                                                                                                                         | 26 |
| 2.3 | Images of the beam beam counter. Leftmost panel shows a single quartz radiator. Center panel shows a completed detector. Right panel shows the BBC around the beam line. Image taken from [14]. . . . .                                                                                                                                                                                 | 28 |
| 2.4 | The zero degree calorimeter. Image taken from [15]. . . . .                                                                                                                                                                                                                                                                                                                             | 28 |
| 2.5 | The left panel shows the energy deposited in the ZDC versus the total charged detected in BBC in 5% bins (clock method). The right panel shows the same axes but with the BBC method. Image taken from [16].                                                                                                                                                                            | 29 |

|      |                                                                                                                                                                                                                                                                                                                                                                                          |    |
|------|------------------------------------------------------------------------------------------------------------------------------------------------------------------------------------------------------------------------------------------------------------------------------------------------------------------------------------------------------------------------------------------|----|
| 2.6  | Drift chamber configuration with the entire assembly in the left panel. The center panel shows a side view of a sector, and the right panel shows the wire orientations as viewed from above. Image taken from [17]. . . . .                                                                                                                                                             | 30 |
| 2.7  | One of the two RICH detectors (east section). Image taken from [18]. . . . .                                                                                                                                                                                                                                                                                                             | 31 |
| 2.8  | A cutaway view of a single PbSc module used in EMCAL. Image taken from [19]. . . . .                                                                                                                                                                                                                                                                                                     | 33 |
| 2.9  | A deconstructed view of a PbGl super module (6x4 array). Image taken from [19]. . . . .                                                                                                                                                                                                                                                                                                  | 34 |
| 2.10 | A mechanical desgin of the sPHENIX experiment. From the inside out it shows the tracking systems, electromagnetic calorimeter, inner hadronic calorimeter, the solenoid magnet, and outer hadronic calorimeter. Image taken from [20]. . . . .                                                                                                                                           | 35 |
| 2.11 | The left panel shows a mechanical desgin of the electromagnetic calorimeter sector and its towers. The right panel shows a tower assembly with silicon light guides. Image taken from [11]. . . . .                                                                                                                                                                                      | 36 |
| 2.12 | A transverse cutaway of a single outer hadronic calorimeter module. The pink lines are depitced as the absorber plates and the green and blue line show the $12^\circ$ tilt with respect to the radial direction. Image taken from [11]. . . . .                                                                                                                                         | 37 |
| 2.13 | A transverse cutaway of a single inner hadronic calorimeter module. Image taken from [21]. . . . .                                                                                                                                                                                                                                                                                       | 38 |
| 3.1  | Cartoon drawing of a particle identification for the two-particle correlation. $\phi^{Trig}$ . is the trigger particle, $\phi^{Asso}$ . is the associated particle, and $\Delta\phi$ is the angle between the two-particles. $\phi_s$ and $Psi_2$ are the angle of $\phi^{Trig}$ . with respect to the event plane, and event plane itself, respectively. Image taken from [24]. . . . . | 44 |
| 3.2  | An illustration of the jet peaks (red) sitting on top of the background (orange). $b_0$ is the background level. Image taken from [25]. . . . .                                                                                                                                                                                                                                          | 45 |
| 3.3  | A cartoon illustration of the underlying gaussian distributions of the jet peaks. Figure is not drawn to scale. . . . .                                                                                                                                                                                                                                                                  | 47 |
| 4.1  | $\pi^0$ -charged hadron correlation function for Run15 $p+p$ collisions at 200 GeV. The red line is the fit for data and the blue line is the background level. . . . .                                                                                                                                                                                                                  | 49 |
| 4.2  | $\pi^0$ -charged hadron jet function for Run15 $p + p$ at 200 GeV. . . . .                                                                                                                                                                                                                                                                                                               | 49 |
| 4.3  | $\pi^0$ -charged hadron correlation function for Run14 MB data set, 40-45% centrality. The red line is the fit to the data and the blue line is the background from the ZYAM method. . . . .                                                                                                                                                                                             | 50 |
| 4.4  | $\pi^0$ -charged hadron jet function of Run14 MB data set, 40-45% centrality. After the background was removed from 4.3, we see a significant amount of noise between zero and $\pi$ . . . . .                                                                                                                                                                                           | 51 |
| 4.5  | The hot tower maps of EMCAL for Run14. Each panel is a sector, and each sector has axes of tower position along the beam line on the x-axis, and the tower height on the y-axis. . . . .                                                                                                                                                                                                 | 53 |

|      |                                                                                                                                                                                                                                                                                           |    |
|------|-------------------------------------------------------------------------------------------------------------------------------------------------------------------------------------------------------------------------------------------------------------------------------------------|----|
| 4.6  | $R_I$ plotted versus $z_T$ for the 40-45% centrality class, where $z_T$ is the ratio of the partner-to-trigger $p_T$ . The constant fit is over the range of $0.5 < z_T < 1.15$ . . . . .                                                                                                 | 54 |
| 4.7  | $R_I$ versus centrality classes from 40-90% in 5% bins. This plot is not fully corrected, and therefore is not a final result of any kind. . . . .                                                                                                                                        | 55 |
| 4.8  | A plot of arbitrary $R_I$ suppression at high $z_T$ versus the number of participating nuclei ( $N_{part}$ ) for three different systems: Run10 $^3He + Au$ (green) and $Cu + Au$ (red), and Run14 $Au + Au$ (magenta). . . . .                                                           | 56 |
| 4.9  | $\pi^0$ -charged hadron correlation function for Run16 MB data set, 45-50% centrality. The red line is the fit to the data and the blue line is the background. . . . .                                                                                                                   | 57 |
| 4.10 | $\pi^0$ -charged hadron jet function of Run16 MB data set, 45-50% centrality. After the background was removed from Figure 4.9, we see a significant amount of noise between zero and $\pi$ . . . . .                                                                                     | 58 |
| 4.11 | The hot tower maps of EMCAL for Run16. Each panel is a sector, and each sector has axes of tower position along the beam line on the x-axis, and the tower height on the y-axis. . . . .                                                                                                  | 59 |
| 4.12 | $R_I$ plotted versus $z_T$ for the 45-50% centrality class, where $z_T$ is the ratio of the partner-to-trigger $p_T$ . The constant fit is over the range of $0.5 < z_T < 1.15$ . . . . .                                                                                                 | 60 |
| 4.13 | $R_I$ versus centrality classes from 40-90% in 5% bins. . . . .                                                                                                                                                                                                                           | 61 |
| 5.1  | An energy distribution for the outer hadronic calorimeter. This histogram is from $\phi$ -integrated eta bin number 11, which is close to $\eta=0$ in pseudorapidity. . . . .                                                                                                             | 67 |
| 6.1  | Left panel: Monte Carlo output results from Eq. 6.1 is the red data, and the energy shifted results in blue. The x-axis extends to 10, but for a better visual we used a zoomed in image. Right panel: The average $C_{adj,shift}$ value over 5 trials. . . . .                           | 71 |
| 6.2  | Left panel: Monte Carlo output results from Eq. 6.1 is the red data, and the energy shifted results in blue. The x-axis extends to 10, but for a better visual we used a zoomed in image. Right panel: The average $C_{adj,shift}$ value over the 5 trials. . . . .                       | 72 |
| 6.3  | Left panel: Monte Carlo output results from Eq. 5.4 is the red data, and the energy shifted results in blue. The x-axis extends to 10, but for a better visual we used a zoomed in image. Right panel: The average $C_{adj,shift}$ value over the 5 trials of the shifted energy. . . . . | 73 |
| 6.4  | Left panel: Monte Carlo output results from Eq. 5.4 is the red data, and the energy shifted results in blue. The x-axis extends to 10, but for a better visual we used a zoomed in image. Right panel: The average $C_{adj,shift}$ value over the 5 trials. . . . .                       | 73 |
| 6.5  | Plotted is the energy deposition at approximately $\eta = 0$ , so directly above the collision vertex (see Figure 1.4). The y-axis is in logarithmic arbitrary units and the x-axis is energy in GeV. The red fit has a range of 0.02-0.1 GeV, and the teal fit from 0.1-1 GeV. . . . .   | 75 |



# 1 Introductions

As we know, virtually all matter we encounter is comprised of particles called protons, neutrons, and electrons. Understanding the structure of such particles is the study of particle physics, which unveils the most fundamental building blocks of matter. Since the mid 20th century physicists have discovered that protons and neutrons alike are not the underlying particles that make up matter. Particles such as gluons and quarks are what actually make up protons and neutrons. As time has progressed the physics community has unveiled many other types of particles that exist which are made of these quarks. The Standard Model was then invented in order to describe how all the particles fit together, ranging from mass to the kind of force they pertain to. A summary of the Standard Model can be seen in Figure 1.1.

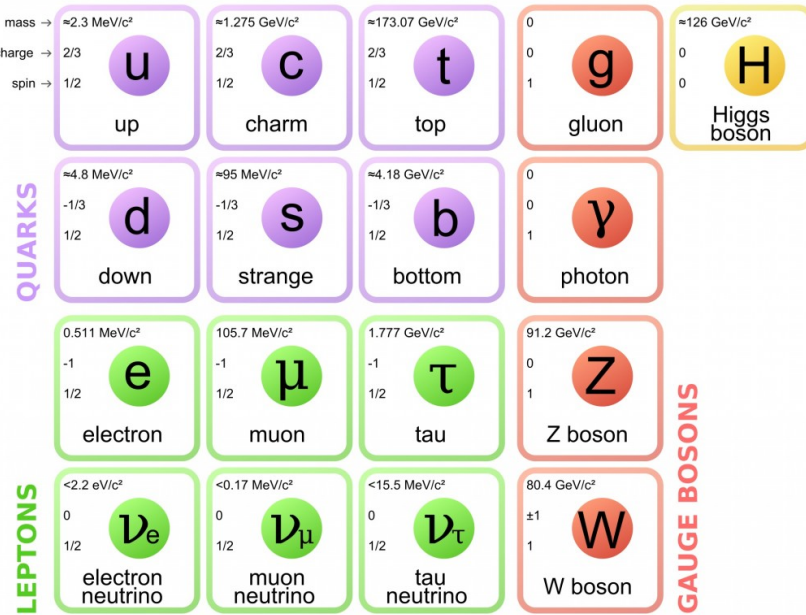


Figure 1.1: Quarks (purple) are the building blocks of hadrons that appear in six flavors. Leptons (green) are half-integer spin particles (fermions), that may be charged like that of the electron or neutral like that of a neutrino or neutron. Bosons are force mediators, and the Higgs boson is how fermionic matter is given mass. Image taken from [1].

## 1.1 Fundamental Forces

Four fundamental forces exist in the universe: the strong nuclear force, weak nuclear force, electromagnetic force, and gravitational force. These forces have particles that mediate, or propagate, their own forces respectively. For example, gluons mediate the strong nuclear force, and photons mediate the electromagnetic force. In this introduction we will give a brief summary of the strong force, and negate the other three for the sake of relevance to the study. A summary of the forces and their mediating particles are given in Table 1.1.

Table 1.1: A summary of the four forces and their respective theory, particle mediator, and range of the force.

| Interaction     | Theory                  | Mediator     | Mass(GeV/c <sup>2</sup> ) | Range(m)          |
|-----------------|-------------------------|--------------|---------------------------|-------------------|
| Strong          | Quantum Chromodynamics  | gluon        | 0                         | 10 <sup>-15</sup> |
| Weak            | Quantum Flavordynamics  | $W^\pm, Z^0$ | 80.4, 91.2                | 10 <sup>-18</sup> |
| Electromagnetic | Quantum Electrodynamics | photon       | 0                         | $\infty$          |
| Gravity         | General Relativity      | graviton     | 0                         | $\infty$          |

### 1.1.1 Strong Nuclear Force

The theoretical framework of the strong force is termed as quantum chromodynamics (QCD), where chromo is derived from the term color. The strong nuclear force can be defined as a force that binds nucleons (protons & neutrons) together which is made possible by gluons. The gluon, which is a massless vector boson, is exchanged between nucleons and partons (quarks and gluons) at a short range, which is on a scale of femtometers. There are eight gluon states which come from the fact that gluons carry color (equivalent to electrons carrying charge). The colors, which does not mean the actual meaning of color in everyday life, are termed red, blue, and green, each having its own 'anti' partner, i.e, anti-red. Gluons can only exist in color neutral pairs such as  $r\bar{b}$ , or  $r\bar{g}$ , and cannot exist freely, which would actually make

the ninth state (nine from the 3 colors and 3 anticolors). The idea of a free gluon (the singlet state) can be compared to that of a photon, but only in the meaning of a isolated particle. Experiments have never observed free gluons as expected from the theory of color charge confinement [2].

Like gluons, quarks cannot exist as free particles either. Quarks are particles that make up constituent matter we see everyday. They come in six *flavors*: up (*u*), down (*d*), strange (*s*), charm (*c*), top (*t*), and bottom (*b*). See Table 1.2 for brief quark summary. Each quark has its own antiparticle as well. Moreover, each quark comes in three colors (red, blue, and green), so there are 36 in all.

Table 1.2: The six types of quarks and their respective charge and mass.

| Quark   | Charge ( <i>e</i> ) | Mass (MeV/c <sup>2</sup> ) |
|---------|---------------------|----------------------------|
| up      | +2/3                | 1.7 - 3.1                  |
| down    | -1/3                | 4.1 - 5.7                  |
| charm   | +2/3                | 1290                       |
| strange | -1/3                | 100                        |
| top     | +2/3                | 4190                       |
| bottom  | -1/3                | 172,900                    |

Combining quarks gives an array of different particles that have been observed in experiments throughout the 20th & 21st century. Particles that are made of a quark-antiquark pair are called *mesons* while particles made of three quarks are called *baryons*. Mesons and baryons fall into the hadron family, which are simply particles made of two or more quarks.

## 1.2 Relativistic Hardon Collisions

### 1.2.1 Event Evolution

At the Relativistic Heavy Ion Collider (RHIC) particles are accelerated to over 99% the speed of light. At this speed particles are Lorentz contracted due to special relativistic effects. Instead of the particles being spherical in shape as they travel, they

become more oblate perpendicular to the direction of travel, and appear more disc-shaped (see Figure 1.2). As the two incoming particles collide they begin to 'melt' in that partons become pseudo-free over the volume of created fireball of released energy. During this process a state of matter called the quark-gluon plasma (QGP) forms. After this the "free" partons recombine to form hadrons that are eventually detected and used in analyses.

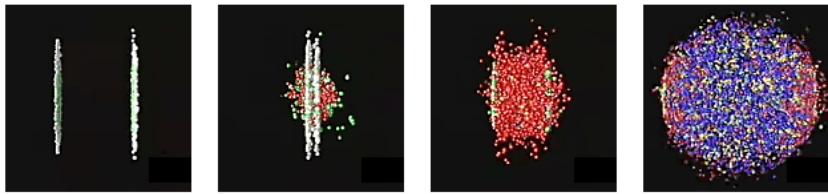


Figure 1.2: The leftmost panel shows two flattened gold nuclei about to collide. The left-center panel shows the initial collision. The right-center panel now shows freed partons. The rightmost panel shows the formation of the quark-gluon plasma. Image taken from [3].

### 1.2.2 Centrality

Heavy-ion collisions have very small impact parameters ( $b$ ) that are difficult to determine. The impact parameter is the distance between two bodies' center's that are interacting, and in heavy-ion physics it may be on the scale of femtometers. So, instead of attempting to measure  $b$ , we describe the collision based on a centrality class. Simply put, a perfect central collision is one where the cross sections of two objects have 100% overlap, or where  $b$  is zero. A very peripheral collision is one where perhaps the far-most edges of the particles overlap and  $b$  is large. At PHENIX, a way to determine centrality is based on the number of particles produced in an event, where the most central collisions produce the most particles, or have a high multiplicity, and more peripheral collisions do not. More so, using the amount of charge deposited into a system of detectors will be of help as well, as we will see in Section 2. See Figure 1.3 for a more elaborate depiction of centrality in heavy-ion physics.

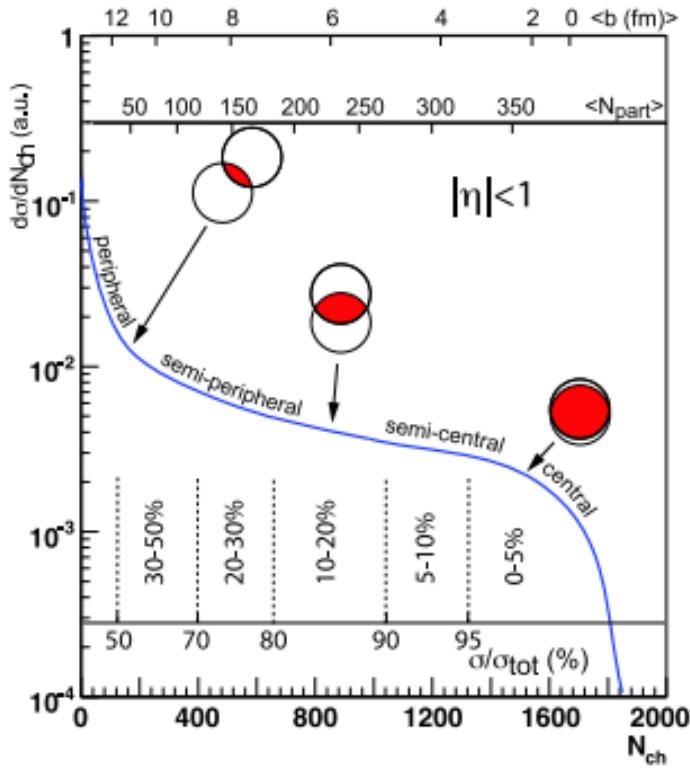


Figure 1.3: A cartoon plot of centrality classes along with other signatures of centrality classes such as number of participating particles,  $\langle N_{part} \rangle$ , charged particle multiplicity  $\langle N_{ch} \rangle$ , and impact parameter,  $b$ . Image taken from [4].

### 1.2.3 Coordinate System

In particle physics several different coordinate systems may be used to determine tracks of particles. It is common though to use coordinates that can track particles with respect to the beam line, which simplifies work. In this experiment we used a coordinate system that defines the location of a particle by the standard polar coordinate  $\phi$  ( $0 \rightarrow 2\pi$ ) and  $\eta$  ( $-\infty \rightarrow \infty$ ), where  $\eta$  is called pseduorapidity.  $\eta$  is defined as

$$\eta = -\ln(\tan(\theta/2)) \quad (1.1)$$

where  $\theta$  is the angle between the beam line. As seen in Figure 1.4,  $\phi$  tracks around

the beam line while  $\eta$  tracks along it.

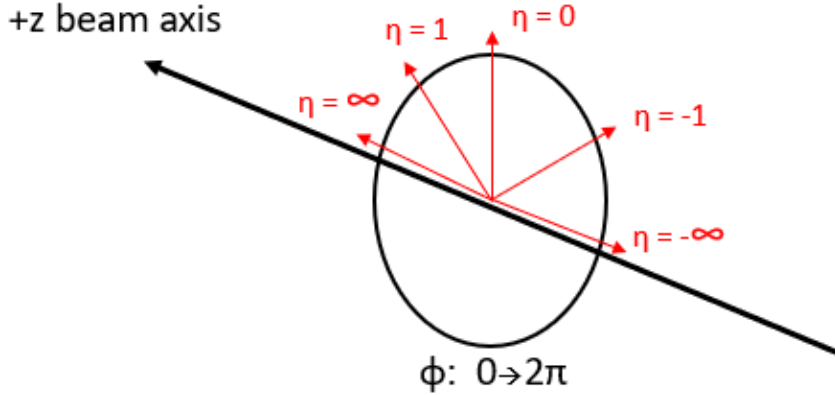


Figure 1.4: Cartoon drawing of the coordinate system used in this study, and common among accelerator physics.  $\eta$  can extend from  $-\infty$  to  $+\infty$ . This study sees the pseudorapidity extend from -1.1 to 1.1.

### 1.3 Quark-Gluon Plasma

The quark-gluon plasma (QGP) is a state of matter that exists only during incredibly hot and dense conditions. Quarks and gluons can move freely, or are unbound to one another in a normal hadronic state. All matter in the universe being in the QGP phase is theorized to have existed shortly after the Big Bang at about  $10^{-5}$  seconds [5], but the QGP quickly cooled and formed hadrons. No other known naturally created sources of the QGP exist, so to study it we recreate it in a laboratory setting. Particle accelerators and colliders can recreate the QGP - RHIC at Brookhaven National Laboratory (BNL), and the Large Hadron Collider (LHC) at the European Organization for Nuclear Research (CERN).

Before confirmation of the recreation of the QGP, several theorized signatures of it were brought forth: harmonic flow, single particle suppression ( $R_{AA}$ ), and jet suppression. This study mainly focuses on using a method called two-prarticle correlations for understanding jet suppression due to the QGP. These signatures of the quark-gluon plasma will be briefly mentioned below.

### 1.3.1 Flow

During most high energy particle collisions we know, the QGP is formed. Once the plasma is formed it does not move in a isotropic fashion. Instead, the plasma may flow with an elliptical shape, or triangular shape. These different types of flow are defined as the flow coefficients. Due to this study not being focused on flow, I will simply give the definition of flow coefficients as

$$\nu_n = \langle \cos(n(\phi - \Psi_{RP})) \rangle \quad (1.2)$$

where  $n$  is the harmonic number ( $n=1,2,3$ , etc.) of the reaction plane angle,  $\phi$  is the azimuthal angle of the outgoing particle after the collision, and  $\Psi_{RP}$  is the reaction plane angle. When  $n = 1$  this is called directed flow,  $n = 2$  is elliptic flow, and  $n = 3$  is triangular flow. Harmonic numbers may go above 3 but is seldom mentioned. The reaction plane angle is made with the beam axis and the impact parameter as show in Figure 1.5.

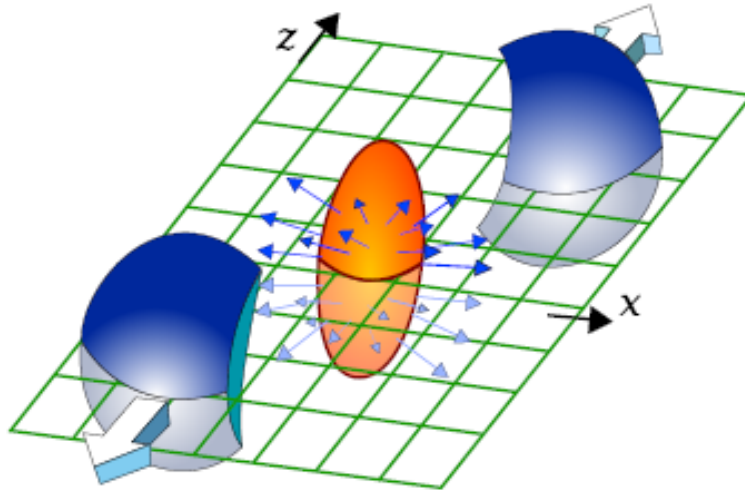


Figure 1.5: A cartoon drawing of two-particles colliding (blue), and the quark-gluon plasma (orange) undergoing flow. The reaction plane is the green grid. Image taken from [6].

### 1.3.2 Jet Quenching

In heavy-ion collisions we know energy and momentum must be conserved, so when two particles (or when a myriad of them) collide most of the final state trajectories have transverse momentum,  $p_T$ . Now, at the time the QGP is present some very high  $p_T$  particles must traverse the medium. A small concentration of high  $p_T$  particles exit the medium as an energetic jet, which usually occurs as two simultaneous jets called di-jets. But one jet usually must travel a shorter distance through the medium, which is called a near-side jet, while the other jet is called the away-side jet. The idea that one or both jets may emerge from the plasma relatively unscathed is called surface bias. But other times a jet may emerge from the surface of the plasma and the other jet directed into the medium. When this happens we say the away-side jet is seen with a large suppression of energy due to the medium, otherwise known as jet quenching. Lastly, partons that serve as the parent of jets may emerge from deep within the plasma, causing both jets to lose some or most of their energy.

#### 1.3.2.1 $R_{AA}$ Single Particle Suppression

In collisions with large nuclei, such as  $Au + Au$ , there is a suppression of particle production at high momenta compared to the rate of particle production expected from  $p + p$  collisions. The observable that can describe this phenomena is called  $R_{AA}$  and can be defined as

$$R_{AA} = \frac{1}{N_{coll}} \frac{d^2 N^{AA}/dydp_T}{\langle T_{AA} \rangle d^2 \sigma_{pp}/dydp_T} \quad (1.3)$$

where  $N_{coll}$  is the number of nucleon-nucleon collisions,  $d^2 N^{AA}$  is the yield of the  $Au + Au$  collision,  $d^2 \sigma_{pp}/dydp_T$  is the  $p + p$  cross section, and  $\langle T_{AA} \rangle$  is the nuclear thickness function based on a Glauber model [7]. In  $p + p$  events we expect the value of  $R_{AA}$  to be one, given that we use it as a baseline for higher nucleon collisions.

So, the evidence for QGP formation is the decrease in  $R_{AA}$  in larger systems as  $p_T$  increases. Figure 1.6 shows  $R_{AA}$  values among different particles, and note that the photon data is not suppressed because photons do not interact with the strong force. The  $\pi^0$  will be a focus in this study, and is commonly created in high energy collisions. In fact, we see the suppression of the  $\pi^0$  production because of the QGP medium.

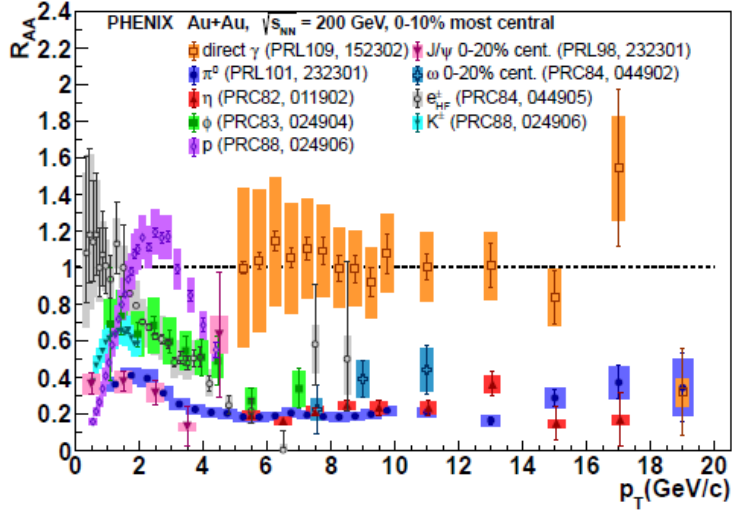


Figure 1.6: A PHENIX plot of  $R_{AA}$  as a function of  $p_T$ . Many different particles are plotted, but most importantly are the  $\pi^0$ 's as they are the trigger in this study. Image taken from [8].

### 1.3.2.2 Two-particle Correlation

Two-particle correlations will be used often in this study. The correlation process can simply be explained as first identifying a particle, in this study a  $\pi^0$ , that has  $p_T$  above about 3 GeV/c. The  $\pi^0$  is then denoted as the *trigger* and then we correlate the angular distribution of associated particles (particles that occur in the same event),  $\Delta\phi$  (see Figure 1.7). Particles with  $p_T$  of 3 GeV/c and greater usually are indicative of a being part of a jet.

When  $\Delta\phi$  is, or close to, zero, the two particles are associated in the same region of space, so belonging to the near-side jet. The near-side jet is also associated with having the smallest pathlength while traversing the QGP. The distribution around

$\Delta\phi=0$  is Gaussian-like, and has been fitted that way in a traditional sense. Then, if particles have a  $\Delta\phi$  of  $\pi$  they belong to the away-side jet. This method will be further discussed in Section 3.4.

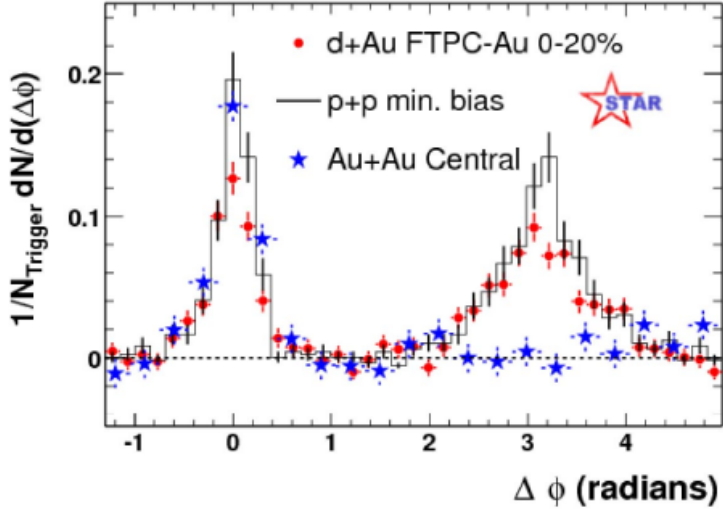


Figure 1.7: Two-particle correlation plot from the STAR collaboration of  $p+p$  (black),  $d + Au$  (red), and  $Au + Au$  (blue). Trigger particles with  $4 < p_T^{\text{trig}} < 6$  GeV/c, and partner particles with  $2 < p_T^{\text{assoc}} < p_T^{\text{trig}}$  GeV/c. Notice the away-side jet suppression for gold at the value of  $\pi$ , it is indicative of the quark-gluon plasma. Image taken from [9].

## 1.4 Motivation of Thesis

This project is dedicated to two different concepts. The first is developing a framework for determining the jet correlation function using PHENIX's Run14 and Run16 data sets, with the ultimate aim, outside the scope of the thesis itself, of showing a high precision double ratio,  $R_I$ , and showing how  $R_I$  changes with centrality. The important ideas for this first concept is to show the statistical significance, or feasibility, of the jet function (as well as the correlation function) in both data sets, along with using the developed framework for studying the systematics in the datasets that need addressed.

The second concept is constructing tools to develop and study the systematic effects and statistical feasibility for performing part of the calibration of the calorimeter

detectors in the new upgraded experiment under development at Brookhaven National Laboratory called sPHENIX. Specifically, we want to develop tools to calibrate three calorimeters to ultimately derive a relative calibration for each detector. We expanded this concept by developing a Monte Carlo simulation to test our tools, ultimately giving more insight to determine the best strategy to calibrate the detectors.

This thesis is developed in a typical fashion with the first section being an introduction of relevant topics of particle physics and relativistic heavy-ion collisions. The second section describes both experiments and relevant detector systems. Then, the analysis and results are reported for the PHENIX study in Sections 3 and 4, respectively. The second analysis and results are on the calibration study of sPHENIX which are Sections 5 and 6, respectively. Finally, we give a summary and future work.

## 2 Experimental Details

### 2.1 Introduction

In this section we describe the experimental facility used for this study. Then we give details of the detector subsystems that are relevant for the topics at hand and a condensed version of how they operate. Two experiments are described here: PHENIX and sPHENIX.

### 2.2 Relativistic Heavy Ion Collider

The Relativistic Heavy Ion Collider (RHIC) is located at Brookhaven National Lab (BNL) in Upton, New York. RHIC consists of two storage rings, 3.86 km in circumference as seen in Figure 2.1. Experiments at RHIC are also labeled in the figure, such as STAR. One purpose of the collider is to accelerate heavy-ion beams (in this study, *Au* particles) near the speed of light and smash them together. These collisions, albeit small on a human scale, produce enormous amounts of energy in a very small region of space. In other words, the energy density is very high. During the moments of particle interactions the quark-gluon plasma (QGP) is created. The experiment PHENIX (Pioneering High Energy Nuclear Interaction eXperiment) was designed to search for this exotic state of matter at RHIC and study its properties. Several other experiments such as BRAHMS, PHOBOS, and STAR were implemented at RHIC, but were not used in this study. From 2000-2016 PHENIX was used to study collisions from a variety of particle interactions from protons, deuterium, helium-3, copper, aluminum, gold, etc.

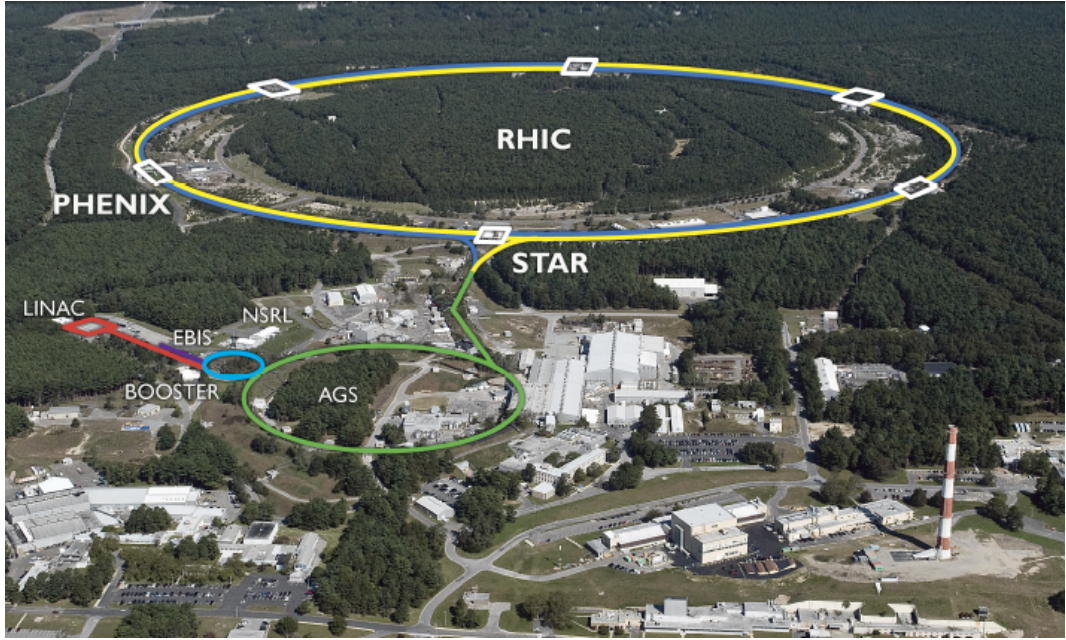


Figure 2.1: An aerial view of the RHIC complex at BNL. The yellow and dark blue lines represent the beam lines. STAR and PHENIX are experiments set up along the beam line, and other labels are smaller accelerators that eventually lead to the large beamlines. Image taken from [10].

A new experiment called sPHENIX is to supersede that of PHENIX. sPHENIX, where the 's' references the *strong* interaction that is studied is designed to measure jets and Upsilon states to determine the temperature dependence of transport coefficients of the QGP [11].

### 2.3 PHENIX

PHENIX was an experiment to study the structure of the QGP, and a myriad of subsystem detectors were used to collect data from particle collisions (see Figure 2.2). PHENIX is devised into two separate arms, or areas that hold detector systems, the central & muon arm. For this study the muon arm is not used so I will not spend time explaining it. For the central arm, the detectors cover an area of  $\pm 0.35$  in  $\eta$  and  $-0.57 \leq \phi \leq 0.97$  to  $2.14 \leq \phi \leq 3.72$  in radians. In the following sections some

of the more important detectors for this analysis are outlined, with Table 2.1 giving a condensed description.

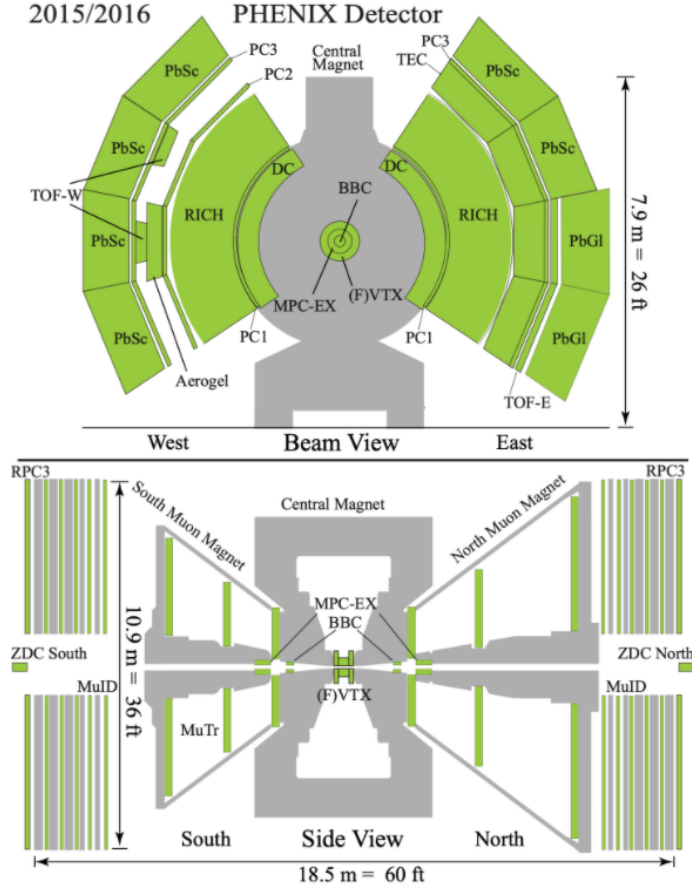


Figure 2.2: PHENIXs Run16 detector configuration as viewed from the beam (top), and from the side (bottom). Image taken from [12].

Table 2.1: A condensed description of PHENIX detectors and their spatial coverage relevant to this thesis. This table is adapted from [13].

| Subsystem                   | $\eta$             | $\phi$          | Summary                                                                                                 |
|-----------------------------|--------------------|-----------------|---------------------------------------------------------------------------------------------------------|
| Central Magnet              | $\pm 0.35$         | $2\pi$          | Bend charged particles.                                                                                 |
| Beam Beam Counter           | 3.1 - 3.9          | $2\pi$          | Measures centrality, collision vertex, and responsible for timing of events                             |
| Zero Degree Calorimeter     | $\pm 2\text{mrad}$ | $2\pi$          | Collision location and centrality                                                                       |
| Drift Chamber               | $\pm 0.35$         | $\pi/2$         | Measure position and momentum                                                                           |
| Ring Imaging Cherenkov      | $\pm 3.5$          | $\pi/2$         | Identify electrons                                                                                      |
| Electromagnetic Calorimeter |                    |                 | Measure position and energy of charged particles (and neutrons), identify photons and charged particles |
| PbSc                        | $\pm 0.35$         | $\pi/2 + \pi/4$ |                                                                                                         |
| PbGl                        | $\pm 0.35$         | $\pi/4$         |                                                                                                         |

### 2.3.1 Global Detectors

Global detectors at PHENIX can be thought as event characterization detectors. During an event, or when particles collide, many basic properties are determined by global detectors such as centrality, the collision vertex, start of time of flight (TOF), and trigger <sup>1</sup>.

#### 2.3.1.1 Beam-Beam Counter & Zero Degree Calorimeter

The beam-beam counter (BBC) is a pair of detectors used for charged particle tracking placed around the beam pipe 144 cm away from the geometric center of PHENIX (see Figure 2.3). One is placed on the north side (BBCN) and one on the south side (BBCS). In each of the detectors there are 64 quartz Cherenkov radiators with a Photomultiplier Tube (PMT) attached to it. The essence of the BBC is to determine the collision vertex location, centrality of the collision, and serve as a minimum biased (MB) trigger. The collision vertex is determined by the time it takes a signal to reach both BBCs. With timing resolution on the scale of about 50 picoseconds, the BBC can obtain where a collision took place based on the equation

$$z_{vertex} = c \times \frac{T_S - T_N}{2} \quad (2.1)$$

where  $T_S(T_N)$  is the average hit time for BBCS(BBCN). Collisions that occur with  $z_{vertex} \geq 30$  cm from the center are not collected. From the the amount of charge deposited in the BBC, the centrality class can be determined. For this though, the zero degree calorimeter (ZDC) is used in conjunction with the BBC.

---

<sup>1</sup>Trigger here is defined as a system that determines when to start collecting data based on criteria set in the data acquisition systems.



Figure 2.3: Images of the beam beam counter. Leftmost panel shows a single quartz radiator. Center panel shows a completed detector. Right panel shows the BBC around the beam line. Image taken from [14].

The ZDC is a set of detectors used to collect spectator particles (particles that have not interacted in a collision, or are neutral) on the north and south ends of PHENIX, and also helps serve the MB trigger (see Figure 2.4). The ZDC covers fully in azimuth but only 2 milliradians in  $\eta$ . So, when the BBC has collected a lot of charge and the ZDC collects few spectator particles, we define this as a high centrality collision. The opposite situation would yield a peripheral collision. See Figure 2.5 for a centrality class visual that uses the BBC and ZDC.

The MB triggering is applied when two hits occur in both BBC detectors, and one hit in both ZDCs, as well as when the collision vertex is  $\leq 75$  cm from the geometric center.

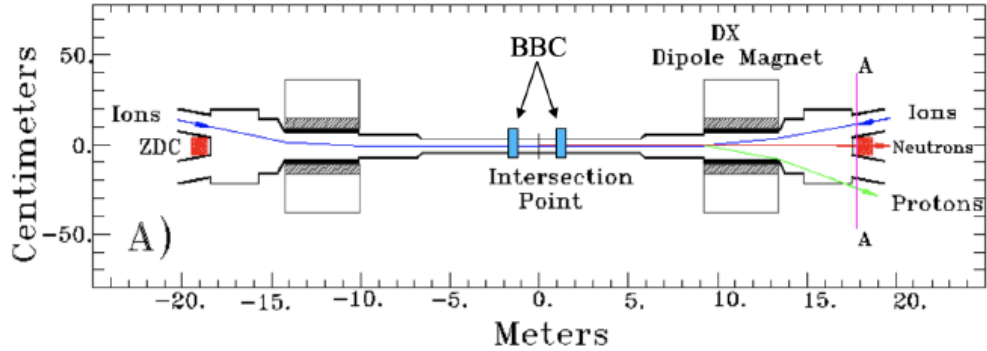


Figure 2.4: The zero degree calorimeter. Image taken from [15].

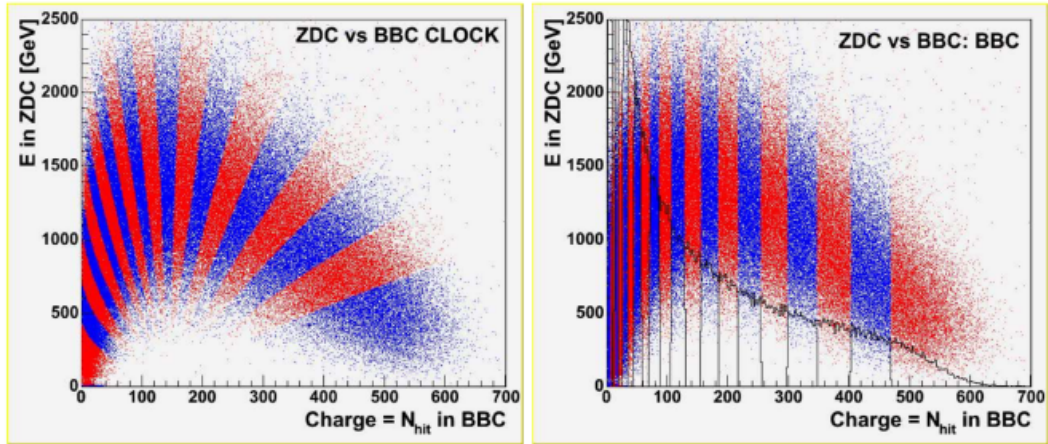


Figure 2.5: The left panel shows the energy deposited in the ZDC versus the total charged detected in BBC in 5% bins (clock method). The right panel shows the same axes but with the BBC method. Image taken from [16].

### 2.3.2 Central Arm Detectors

From Figure 2.2 there is a system of detectors at the heart of PHENIX; we call this area the central arm. Next, a few central arm detectors important to data acquisition for this study are outlined.

#### 2.3.2.1 Drift Chamber

The Drift Chamber (DC) consists of two identical detectors, one on the east arm and one on the west. It is cylindrical in shape, spanning  $90^\circ$  in  $\phi$ , with an inner radius of 2 m, and an outer radius of 2.4 m. They span 2 meters along the z-axis (see Figure 2.6) which places it in a  $\vec{B}$  field of about 0.6kG (kilo-Gauss). This is important for tracking particles. Inside each DC is a gaseous volume of 50% Argone and 50% Ethane and a wire arrangement.

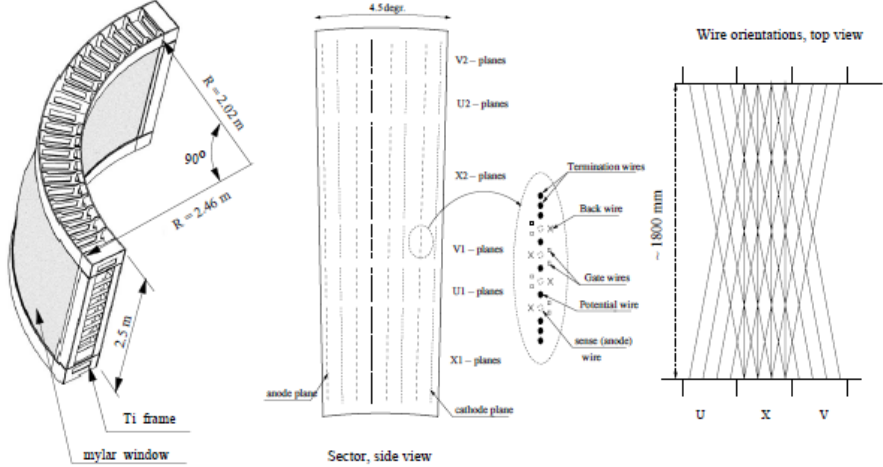


Figure 2.6: Drift chamber configuration with the entire assembly in the left panel. The center panel shows a side view of a sector, and the right panel shows the wire orientations as viewed from above. Image taken from [17].

The purpose of the DC is to contribute to charged hadron tracking. Because DC is in the  $\vec{B}$  field, charged particle tracks are bent, and based on the curvature of the track, identification of the invariant mass of a particle can be determined. For example, when the  $J/\psi$  meson decays into  $e^+e^-$ , the mass of the  $J/\psi$  can be determined from determining the  $p_T$  of the charged track, but of course it is a bit more complex than that. It is not important to fully understand the wire arrangement in Figure 2.6, but the main purpose is to steer electrons from the ionized gas to anodes to then determine the  $p_T$  and charge of the track.

### 2.3.2.2 Ring Imaging Cherenkov Detector

The Ring Imaging Cherenkov Dector (RICH) is a particle identification detector that consists of two PMT arrays and 14 mirrors and resides on each part of the central arm. See Figure 2.7 for a real image of one of the RICH detectors. The total amount of PMTs is 5,120 divided equally among the four arrays. It has the ability to identify charged particle tracks, electrons precisely, due to the gaseous  $CO_2$  volume (index refraction of  $n = 1.00041$ ) that occupies each detector. Electrons pierce

through RICHs CO<sub>2</sub> volume and polarizes the molecules. These molecules align with the magnetic field of the electron, have a brief energy increase, and fall back to the ground state emitting Cherenkov radiation. When the phase velocity of the electrons is higher than  $c$  in the medium the Cherenkov radiation constructively interferes, allowing signals to reach the PMTs. When the phase velocity of the electron is less than that of  $c$  in the medium, the photons destructively interfere, rendering no Cherenkov radiation.

RICH is an essential component to this study as it is able to identify electrons and be crossed checked with an electromagnetic calorimeter (see next Section).



Figure 2.7: One of the two RICH detectors (east section). Image taken from [18].

### 2.3.2.3 Electromagnetic Calorimeter

PHENIX's electromagnetic calorimeter (EMCal) serves the purpose of detecting charged particles and photons, and measuring the position and energy of these par-

ticles. EMCal is the outer-most detector on both sides of the central arm with an acceptance of  $|\eta| < 0.375$  and spanning  $90^\circ$  for each detector. On the west side there are four sectors comprised of lead-scintillator (PbSc) sampling calorimeters, and the east having two sectors of PbSc and two sectors of lead-glass (PbGl) sampling calorimeters.

The fundamental unit of the PbSc detector is called a tower (5.5cm x 5.5cm x 37.5cm). In one tower there exists sixty-six tiles of alternating Pb and Sc connected by wavelength shifting fibers at the front end. The back end of each tower has a PMT where all shifting fibers connect for light collection. How light signals are collected is important enough for a brief explanation. When a charged particle or photon strikes a module it first strikes a Pb tile, which causes an electromagnetic shower. This shower (which is based on the photoelectric effect) will then hit a scintillator tile which generates light. This process then spans across the entire tower, with the signal traveling along a guide to the PMT from a single high voltage that is actually set across 12 modules (LeCroy High Voltage Channel). The light signal is then collected and digitized for further analysis.

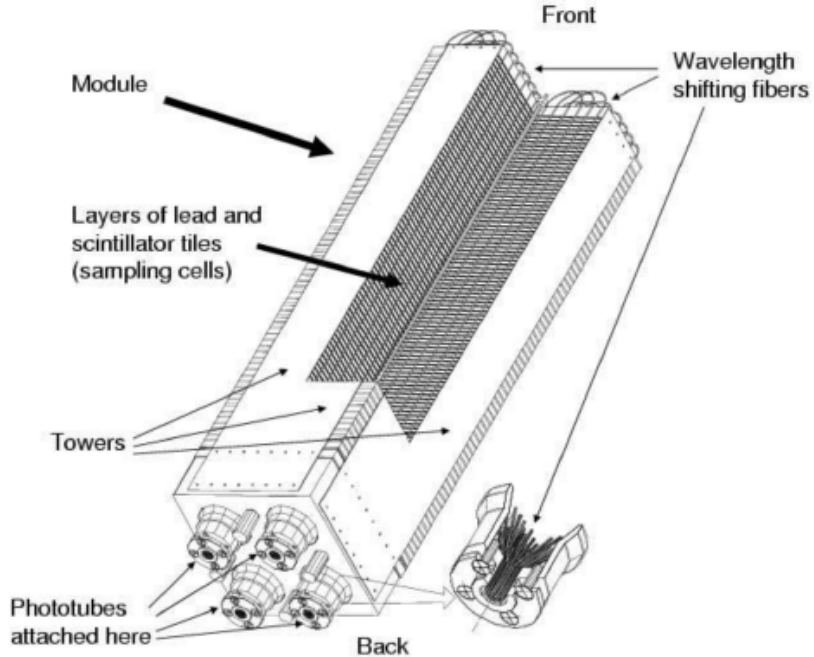


Figure 2.8: A cutaway view of a single PbSc module used in EMCAL. Image taken from [19].

Four towers (in a 2x2 arrangement) form a module as seen in Figure 2.8. A module is really the basic *building block* for EMCAL, and modules are constructed into larger systems. When thirty-six modules are collected in a 6x6 arrangement it is called a SuperModule (SM), and when there is a collection of 18 SMs (6x3 array) it is called a sector. So, for the PbSc there are a total of 15,552 towers (east and west arms).

The basic unit for the PbGl detector (see Figure 2.9) is comparable to that of PbSc in terms of internal mechanism, but slightly different in design. One PbGl detector (4cm x 4cm x 40cm) consists of a homogeneous solid block of Pb, glass, and Pb-Oxide. Instead of collecting light by electromagnetic showering, the PMT in this detector collects light from Cherenkov radiation from electrons. Each detector for PbGl is actually a single module, not a tower, like PbSc, and the PbGl is formed into a SM (6x4 array). One sector for PbGl is formed by 18 SM for a total of 4,608 modules, and 9,216 total modules for both arms.

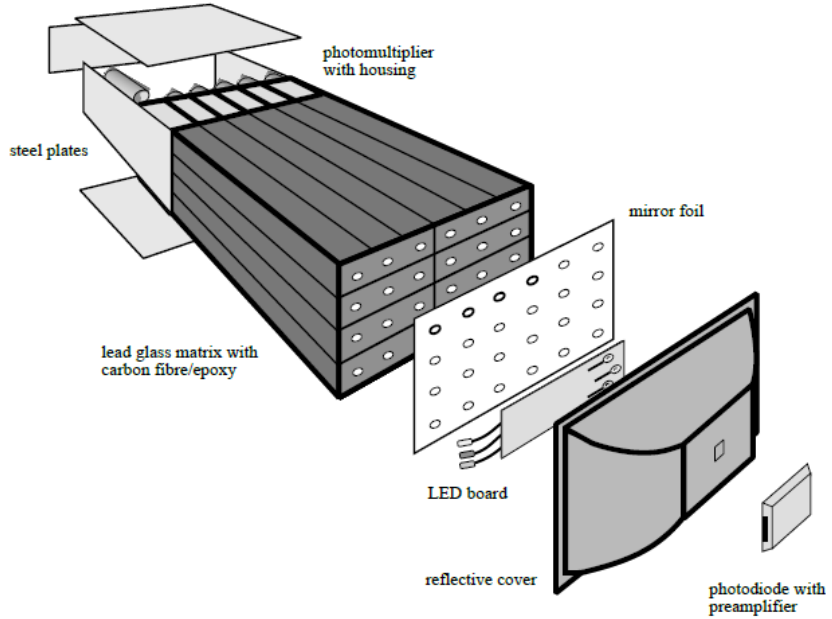


Figure 2.9: A deconstructed view of a PbG1 super module (6x4 array). Image taken from [19].

## 2.4 sPHENIX

As mentioned before, sPHENIX is a new experiment currently in development at RHIC designed to measure jets and Upsilon states to determine the temperature dependence of transport coefficients of the QGP [11] (see Figure 2.10). Most of the hardware from PHENIX is going to be used for sPHENIX, but the latter will use a few new detector systems. For example, the BBC as mentioned in section 2.3.1.1 will be reused, but major systems that are new for sPHENIX are an electromagnetic calorimeter (sEMCal), and an Inner and Outer hadronic calorimeter (IHCal & OHCal, respectively). In this study we will be performing energy calibrations for the three new calorimeter's mentioned above using simulated data.

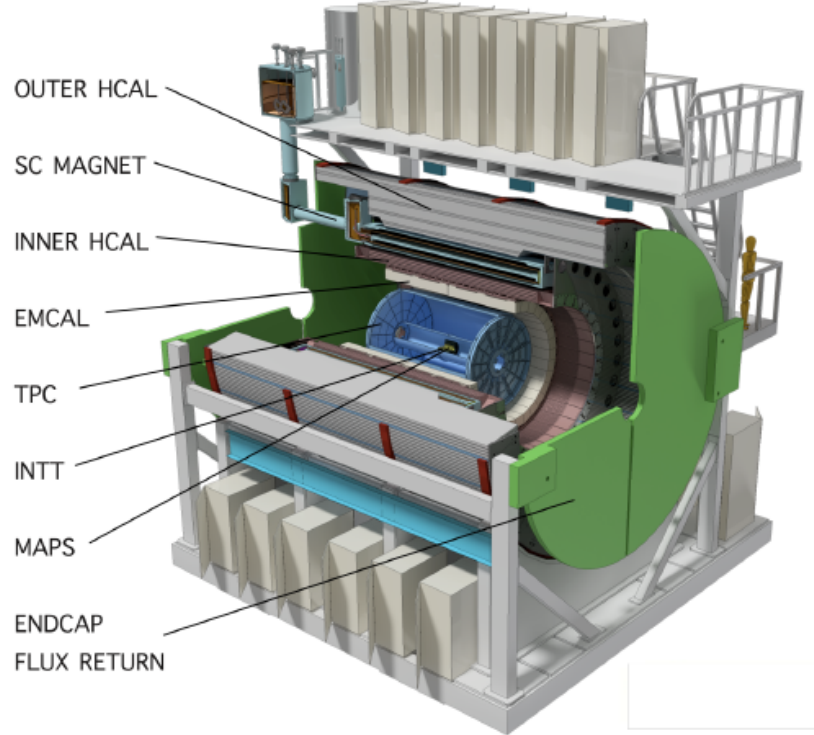


Figure 2.10: A mechanical design of the sPHENIX experiment. From the inside out it shows the tracking systems, electromagnetic calorimeter, inner hadronic calorimeter, the solenoid magnet, and outer hadronic calorimeter. Image taken from [20].

#### 2.4.1 Electromagnetic Calorimeter

The electromagnetic calorimeter for sPHENIX, which I will denote as sEMCal, so as to not be confused by PHENIX's EMCAL, is very similar to that of PHENIX. The purpose of sEMCal is to detect direct photons<sup>2</sup> from a hadronic collision, measure charged particles and photons, and help in jet reconstruction.

sEMCal will have azimuthal coverage of  $2\pi$  in  $\phi$  and an acceptance of  $\pm 1.1$  in  $\eta$ . The inner radius will be set 0.90 m away from the geometric center with the outer radius reaching 1.161 m. Fine segmentation of towers ( $\approx 1.98\text{cm} \times 1.98\text{cm} \times 14.4\text{cm}$ ) in sEMCal has been produced to diminish dead zones and gaps – 24,596 towers will be utilized. The basic building block are literally called *blocks* (see Figure 2.11) which

---

<sup>2</sup>A direct photon originates from hard scattering interactions such as quark-quark, gluon-quark, or gluon-gluon.

are four towers (2x2). Each block has a similar mechanical design to PHENIX's EM-Cal, but here the block is filled with 2,668 scintillating fibers, tungsten powder, and an epoxy. At the end of the block four silicon photomultipliers (SiPM's) are attached and optically coupled to light guides by silicone cookies. The light is then converted to a voltage by an Analog-to-Digital Converter (ADC) and stored.

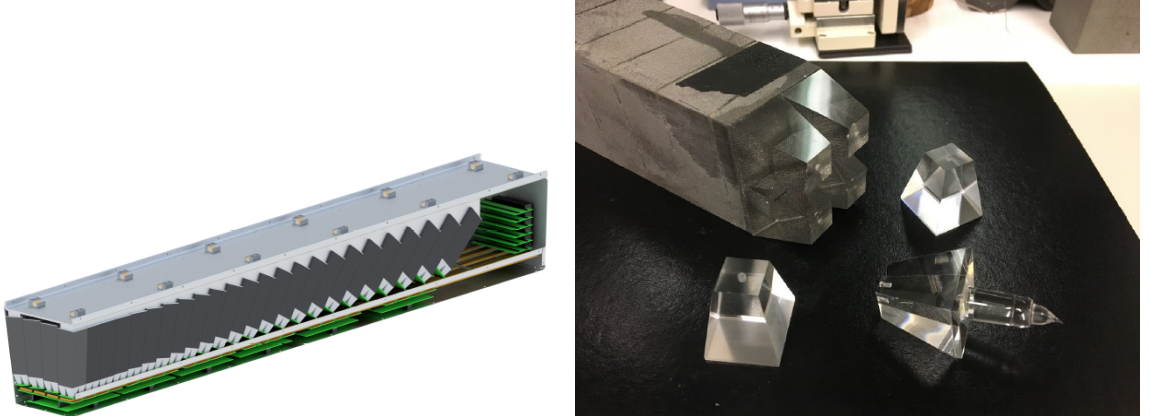


Figure 2.11: The left panel shows a mechanical design of the electromagnetic calorimeter sector and its towers. The right panel shows a tower assembly with silicon light guides. Image taken from [11].

#### 2.4.2 Hadronic Calorimeter

sPHENIX will have a hadronic calorimeter that has two different systems, an inner (IHCal) and outer (OHCAL) calorimeter. IHCal will sit inside the solenoid magnet as seen in Figure 2.10, and the OHCAL just outside the magnet that also serves as the flux return of the solenoid. Both detectors have full azimuthal coverage and an  $\eta$  acceptance of  $\pm 1.1$ . The OHCAL consists of steel absorber plates and scintillator tiles that will collect hadrons and electrons while IHCal consists of aluminum plates and the same scintillator tiles, and also detects hadrons and electrons. When the particles are detected a similar mechanism like that of the sEMCal will convert SiPM energy to a voltage using an ADC. The segmentation of the detector components extend as  $\Delta\eta \times \Delta\phi \approx 0.1 \times 0.1$ .

OHCAL consists of 32 modules, where two towers in  $\phi$  and 24 towers in  $\eta$  are in each module. Towers have 5 tiles being read by SiPMs along the outer radius of OHCAL. The inner radius begins at 1.820 m from the beam line and extends to 2.700 m, with the length of the detector is 6.316 m. The total number of towers is 1536 ( $64\Delta\phi \times 24\Delta\eta$ ) that are tilted  $12^\circ$  relative to the radius to allow tracks to traverse at least four tiles. See Figure 2.12 for a cutaway of an OHCAL module.

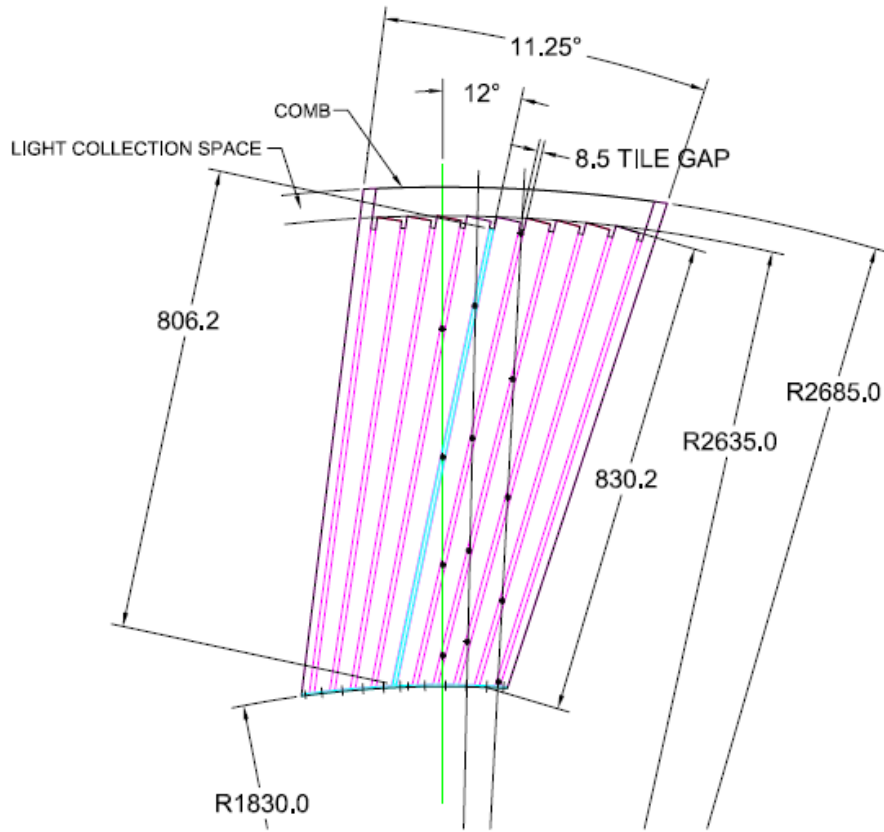


Figure 2.12: A transverse cutaway of a single outer hadronic calorimeter module. The pink lines are depicted as the absorber plates and the green and blue line show the  $12^\circ$  tilt with respect to the radial direction. Image taken from [11].

IHCAL will also consist of 32 modules with the same tower set up as OHCAL, the same number of tiles per tower, and the same number of total towers but with a  $32^\circ$  tilt. The inner radius is 1.157 m from the beam line and extends to 1.370 m with length of 4.350 m. See Figure 2.13.

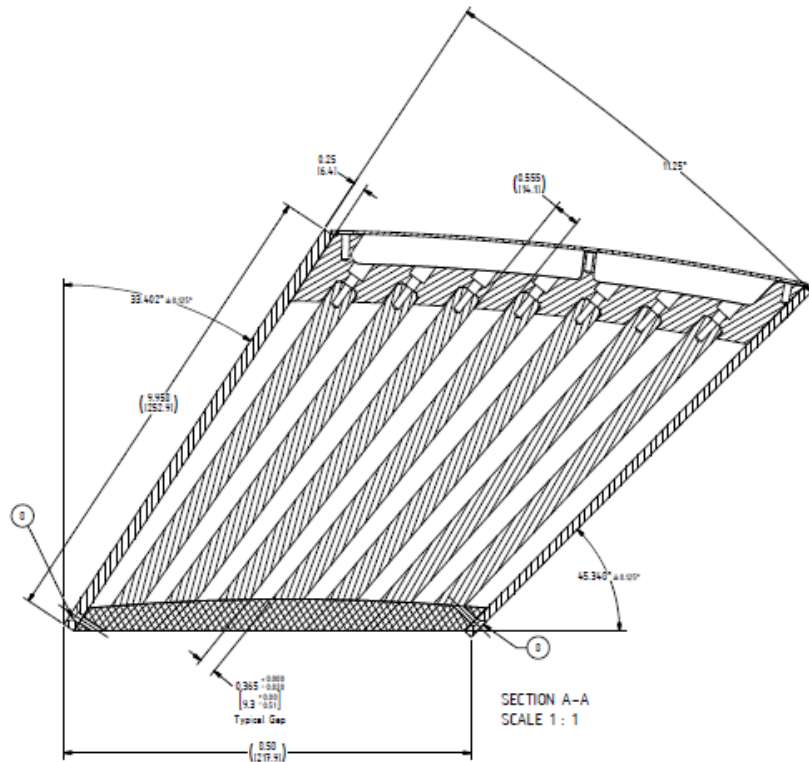


Figure 2.13: A transverse cutaway of a single inner hadronic calorimeter module. Image taken from [21].

### 3 Part I: Development of PHENIX Framework for Studying Two-Particle Correlations and $R_I$ Suppression in Small Centrality Bin Sizes and Small Collision Overlap

#### 3.1 Introduction

This study is about building a framework for analyzing the jet modification behavior in Run14 and Run16 MB data sets. The analysis presented here was accomplished by using a macro framework from previous studies such as [22] and [23], but tended for our runs and centralities, etc. In this section we present the analysis methodology used and further developed as part of this thesis work. The results based on these analysis methods will be presented in Section 4. The plots there are not final results, of course; the point of this thesis is to study the suitability of the data sets and to discover which systematics need addressed to use them. In this way we will see issues that have come about and how they will be fixed in future work.

The development of these tools is specifically focused on assessing the suitability of making a measurement in the smallest collision geometries (most peripheral centralities) with a finer centrality binning and higher precision than ever before at RHIC. The purposes of using finer binning is to see exactly how, and if the jet suppression effect (see Section 1.3.2) turns off as the collision size approaches that of  $p + p$  collisions.

#### 3.2 Run Selection

In this thesis, since our goal is to analyze jets in the QGP, we chose to analyze Run14 and Run16  $Au + Au$  collisions at  $\sqrt{s_{NN}} = 200$  GeV, both with a MB trigger (see Section 2.2.2). Table 3.1 summarizes relevant information for each run used in the analysis.

Table 3.1: Year 2014 and 2016 runs with beam information and the number of events sampled over.

| Run Year | Beam Species | Beam Energy $\sqrt{s_{NN}}$ | Sampled Events     |
|----------|--------------|-----------------------------|--------------------|
| 2014     | Au + Au      | 200                         | $18.5 \times 10^9$ |
| 2016     | Au + Au      | 200                         | $14.4 \times 10^9$ |

### 3.3 Particle Selection

As mentioned before, we use the two-particle correlation method extensively to understand properties of the QGP in  $Au + Au$  collisions, and extracting data pertaining to particles that allow us to analyze the medium is very important. Not only do we want to know which hits are photons versus charged hadrons, but we need to distinguish which are associated with jets.

#### 3.3.1 $\pi^0$ Trigger

We use the  $\pi^0$  meson, which is the lightest of the mesons, as the trigger particle for jet analysis, where trigger does not have the same meaning previously. It means a particle with high  $p_T$ , usually greater than 3 GeV/c (in our analysis  $> 5$  GeV/c), which usually is indicative of a jet. It would be best to use direct photons, which are photons that are produced from hard scattering events, because they do not interact with the QGP, thus the strong force, giving a direct probe on the medium. But, the reason we do not use the direct photons is because they suffer from low statistics, or low signal. What we do instead is use the fact that the  $\pi^0$  decays into two photons with a 98.8% branch ratio,  $\pi^0 \rightarrow \gamma + \gamma$ . This then gives a lot of statistics, hence we choose it to be a trigger particle. The  $p_T$  cut on  $\pi^0$  is 5 GeV/c  $< p_T < 17$  GeV/c, where the upper limit is chosen because the two photons are no longer separable in the EMCAL towers at such a high energy. The lower limit cut reduces the uninteresting events.

To ensure we have detected photons that branch from  $\pi^0$ 's, the invariant mass of

the  $\pi^0$  ( $0.134 \text{ GeV}/c^2$ ) is recreated using the equation

$$m_{\pi^0} = \sqrt{2E_1 E_2 (1 - \cos(\phi_{\gamma_1 \gamma_2}))} \quad (3.1)$$

where  $E_1(E_2)$  is the energy of photon 1(2), and  $\phi$  is the opening angle between the two photons. There is a cut made on the invariant mass where  $0.12 \leq m_{\pi^0} \leq 0.16 \text{ GeV}/c^2$  is kept. The two photon energies mentioned here must also meet the requirement of  $E_\gamma > 1 \text{ GeV}$ . There are more cuts made on the  $\pi^0$ , but they are not significant for discussion in this analysis.

### 3.3.2 Photon Selection

Distinguishing photons in events have a few criteria. First, they must have  $p_T \geq 1 \text{ GeV}$ . Because photons interact with the EMCal, which has over 24,000 towers, some towers are dead, or hot, and we must remove the these from the analysis. Dead towers are towers that simply are not responsive to hits, and hot towers are towers that fire repeatedly due essentially to electronic noise. Section 5 has a brief discussion on hot towers of Run14 and Run16, though the removal of hot/dead towers was not performed in this analysis.

### 3.3.3 Charged Hadron Selection

As mentioned before, the Drift Chamber (DC) has the majority of the track information including momentum and trajectories of charged particles, and in this study we use charged hadrons as partners in the two-particle correlation method. The Pad Chamber (PC), which was not outlined in the Experimental Details section, measures the position of charged particles. Together, along with the EMCal, they contribute to an assessment of the qualities of the other various measurements of the tracks. There are a few criteria charged hadrons meet. The  $p_T$  range for charged hadrons is  $0.5 \leq p_T \leq 10 \text{ GeV}/c$ . Furthermore, there is a criterion called track quality,

where this corresponds to particular hits in the DC and PC. The track quality must be either 63 or 31, where 63 is the highest quality particle track and the latter is the second highest. When charged particles enter the RICH detector with  $p_T > 5$  GeV/c they produce Cherenkov radiation as was already explained in Section 2.2.5, so are kept during data acquisition.

After charged particles, or photons, have traveled through the inner most subsystem detectors, the PC3 and EMCAL will be hit by them. Projections of charged tracks are also placed on PC3 and EMCAL, where tracks are cut using a certain distribution value. When a track is projected on PC3 with the variables of  $\phi$  and  $z$  in use, and when the magnitude of the projection  $\sqrt{\sigma_\phi^2 + \sigma_z^2} \leq 2$  the tracks are accepted. The same idea applies to EMCAL.

### 3.4 $p_T$ and Centrality Selection

In this analysis there are several bin ranges for trigger particles, and separate ones for partner particles. The same selections are used in Run14 and Run16. Also, centrality ranges are the same for each Run and is shown below.

- Trigger Binning: 5-7, 7-9, 9-12, 12-15 GeV/c
- Partner Binning: 0.6-1, 1-2, 2-3, 3-5, 5-7 GeV/c
- Centrality Range: 40-90% in increments of 5%, i.e., 40-45%, 45-50%, etc.

The 5% binning of centrality is smaller than has previously been used in PHENIX or elsewhere at RHIC, especially for these most peripheral bins we are interested in. Part of the purpose of this thesis is to assess the possibility of making smaller centrality binning, possibly as small as 3%. As will be seen in Section 4, this seems

likely to be possible in future work.

### 3.5 Two-Particle Correlation

In large systems such as  $Au + Au$ , reconstructing jets is difficult due to the number of involved particles. Also, there are a lot of lower energy particles in such collisions that serve as an underlying background. So, we rely on high  $p_T$  particles to serve as identifiers of jets. Particles that don't have as high of  $p_T$  that are part of the same event are called partner, or associated, particles (see Figure 3.1). The partner particles are charged hadrons in this analysis. The two-particle correlation can then begin as we correlate the change in  $\phi$  between the trigger and partner particles. Because jets are back-to-back, or separated by  $\pi$ , there will be Gaussian-like peaks around 0 and  $\pi$ . There are issues with the two-particle correlation though, due to PHENIX's limited acceptance  $\phi$ . This issue is fixed by correlating trigger and partner particles of different events which is known as the correlation function, which is defined as

$$C(\Delta\phi) \propto \frac{N_{same}^{AB}(\Delta\phi)}{N_{mix}^{AB}(\Delta\phi)} \quad (3.2)$$

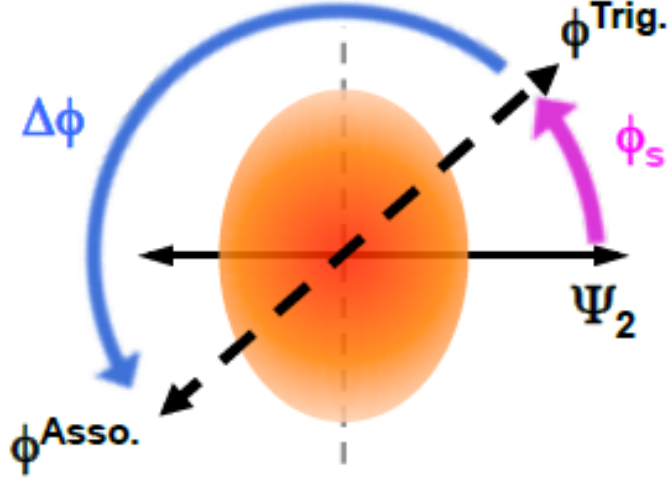


Figure 3.1: Cartoon drawing of a particle identification for the two-particle correlation.  $\phi^{Trig.}$  is the trigger particle,  $\phi^{Asso.}$  is the associated particle, and  $\Delta\phi$  is the angle between the two-particles.  $\phi_s$  and  $\Psi_2$  are the angle of  $\phi^{Trig.}$  with respect to the event plane, and event plane itself, respectively. Image taken from [24].

where  $N_{same}^{AB}$  is the total number of trigger( $A$ ) and partner( $B$ ) pairs from the same event, and  $N_{mix}^{AB}$  is from mixed events. The  $\eta$  acceptance correction will not be brought forth in this analysis.

### 3.5.1 Background and Jet Function

Once the correlation function is obtained, the background level ( $b_0$ ) is subtracted to yield the jet function  $J(\Delta\phi_{AB})$ . The flow contributions briefly introduced at the beginning of this thesis can be removed as well because flow and jets are separable phenomena. The following equation describes this idea as

$$C(\Delta\phi_{AB}) = J(\Delta\phi_{AB}) + b_0 \left[ 1 + \sum_{n=1}^{\infty} \langle 2\nu_n^A \nu_n^B \rangle \cos(n\Delta\phi_{AB}) \right] \quad (3.3)$$

where  $b_0 = \langle n_{bg}^{AB} \rangle / \langle n_{same}^{Ab} \rangle$ . In this analysis the Zero Yield at Minimum (ZYAM) method is used to estimate the background. It is possible for small contributions to be made around the region  $\pi/2$  where we anticipate it to be zero. Despite this,

around  $\pi/2$ , is where we estimate  $b_0$  (see Figure 3.2). Of course, there can be an over, or under, subtraction of the background depending if the jets contribute enough to the background, or the statistics are too low.

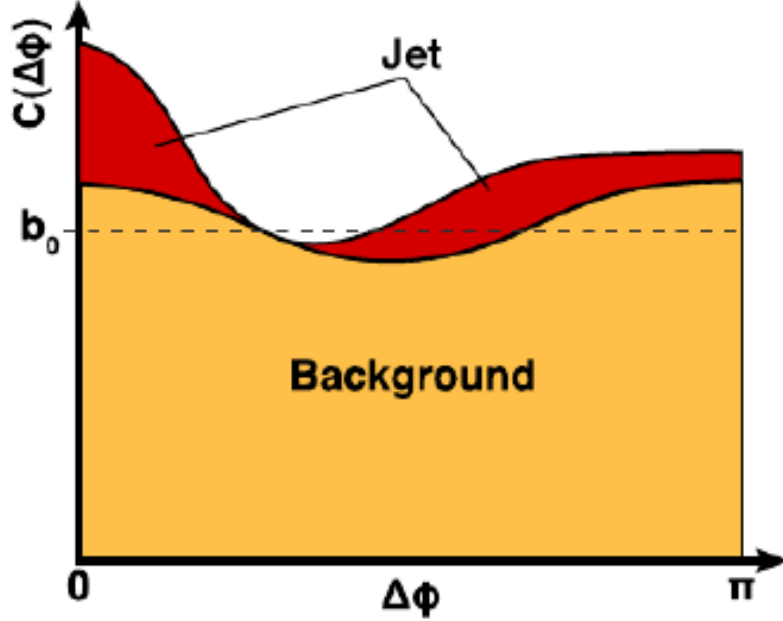


Figure 3.2: An illustration of the jet peaks (red) sitting on top of the background (orange).  $b_0$  is the background level. Image taken from [25].

### 3.6 Double Ratio $R_I$

$R_I$  is a ratio between the  $\Delta\phi$  integrated per-trigger yield ( $Y$ ) of the near and away-side jets. It is a modification of the commonly used variable for jet suppression,  $I_{AA}$ , defined as

$$R_I = \frac{Y_{away}^{AA}/Y_{near}^{AA}}{Y_{away}^{pp}/Y_{near}^{pp}} \quad (3.4)$$

The reason for using  $R_I$  is to eliminate systematic uncertainties such as the limited  $\phi$  and  $\eta$  acceptances in PHENIX. The ratio is minutely sensitive to hadron detection efficiencies because the efficiency is the same for the near and away-side, thus the ratio cancels it.

In the Results section we will see how  $R_I$  changes as a function of  $z_T$ , the ratio of charged hadron (partner) and  $\pi^0$  (trigger)  $p_T$

$$z_T = \frac{p_T^{h^\pm}}{p_T^{\pi^0}} \quad (3.5)$$

More so we will see how these variables change as we reach more peripheral centrality classes. At small  $z_T$  Eq. 3.5 tells us that the  $\pi^0 p_T$  is much larger than the charged hadrons. This indicates that the trigger has little modification from the QGP medium, which also would tell us this is occurring at the surface of QGP (called a surface bias effect). More so,  $R_I$  can sometimes be enhanced because  $Au + Au$  collisions have a larger multiplicity than  $p + p$ . The enhancement comes from a low  $z_T$  background. As  $z_T$  increases, the  $\pi^0$  and hadron have nearly the same  $p_T$ , but if the partner jet traverses the QGP, there is energy loss and less yield from the partners on the away-side will be measured resulting in the before-mentioned suppression.

### 3.6.1 Bleeding Correction

In the two-particle correlation method the peaks at 0 (near-side jet) and  $\pi$  (away-side jet) have slight contamination from each other. In other words, the tail of the near-side Gaussian profile bleeds into the tail of the away-side Gaussian, and vice versa. The correction that is applied is defined as

$$Y_N = \int_0^{\pi/2} JF(\Delta\phi)d\Delta\phi - \int_0^{\pi/2} Gaus_A(\Delta\phi)d\Delta\phi + \int_{\pi/2}^{\pi} Gaus_N(\Delta\phi)d\Delta\phi \quad (3.6)$$

$$Y_A = \int_{\pi/2}^{\pi} JF(\Delta\phi)d\Delta\phi - \int_{\pi/2}^{\pi} Gaus_N(\Delta\phi)d\Delta\phi + \int_0^{\pi/2} Gaus_A(\Delta\phi)d\Delta\phi \quad (3.7)$$

A cartoon example of this bleeding idea is given below in Figure 3.3. The red dotted lines represent the gaussian tail bleeding into each peak. The integration limit of  $\pi/2$  is used under the assumption there is zero background and the correlation function is zero. Note that the peaks seemingly are sitting on a background, but it appears this way for illustrative purposes only.

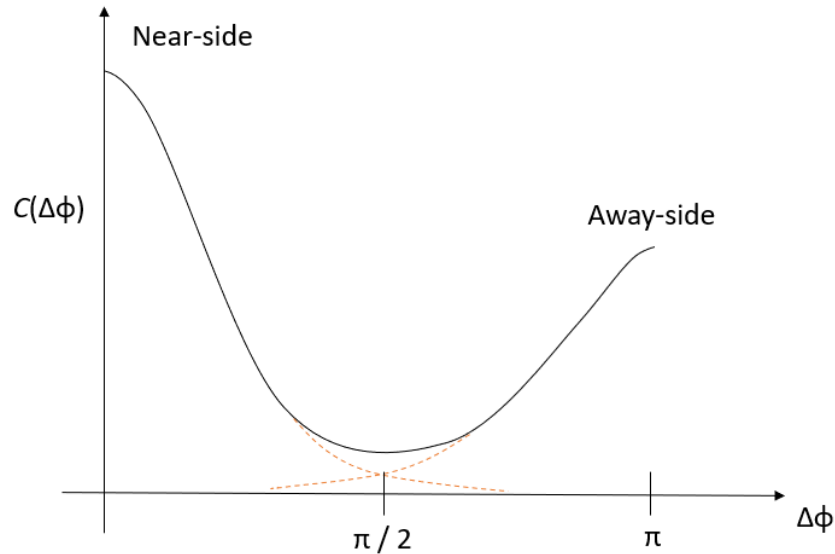


Figure 3.3: A cartoon illustration of the underlying gaussian distributions of the jet peaks. Figure is not drawn to scale.

## 4 Results for Part I: Studies of Systematics and Statistical Precision of Two-particle Correlations and $R_I$ Suppression

In this section we present the results for Run14 and Run16  $Au + Au$  collisions at energies of 200 GeV using PHENIX. Before we present those results, we first introduce a baseline measurement using proton proton ( $p + p$ ) collisions from Run15. It is most ideal to use  $p + p$  baseline measurement because it is the smallest system to collide. Then, enhancements of physical quantities can be seen as a scale in reference to  $p + p$ . After the baseline measurement is presented, Run14 results will be discussed and then Run16.

### 4.1 Baseline Measurement: $p + p$

#### 4.1.1 Correlation & Jet Function

Here we present the  $p + p$  measurements used as a baseline for this analysis. The following plots used data from Run15 at  $\sqrt{s_{NN}} = 200$  GeV. We see the correlation function in multiple  $\pi^0$  trigger and partner bins in Figure 4.1. From top to bottom are  $\pi^0$  bins of 5-7, 7-9, 9-12, and 12-15 GeV/c, and from left to right are partner bins of 0.6-1, 1-2, 2-3, 3-5, and 5-7 GeV/c. Each x-axis has the units of  $\Delta\phi$ .

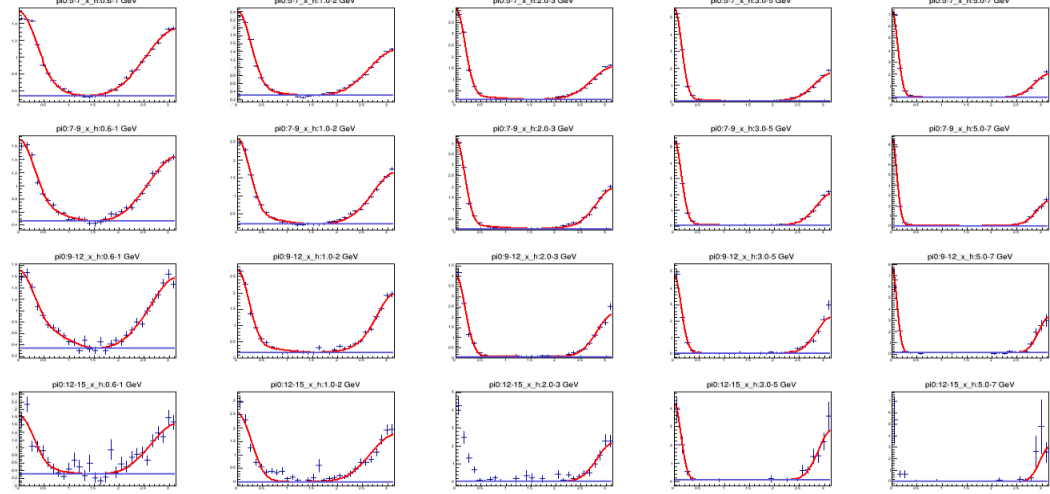


Figure 4.1:  $\pi^0$ -charged hadron correlation function for Run15  $p + p$  collisions at 200 GeV. The red line is the fit for data and the blue line is the background level.

In Figure 4.1, we see peaks at zero and  $\pi$  which corresponds to the near and away-side jet peak, respectively. After using the ZYAM background method, we obtained the jet function as seen in Figure 4.2. Run15 had a large amount of statistics, yielding a high quality correlation and jet function among most trigger-partner bins. It is evident that even in small systems there is a suppression to the away-side jet as there is a smaller value of the jet function.

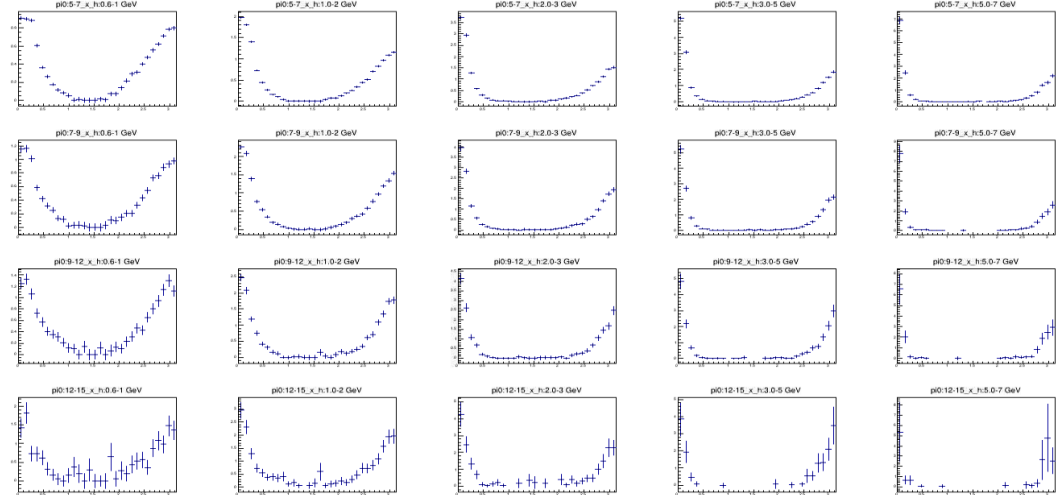


Figure 4.2:  $\pi^0$ -charged hadron jet function for Run15  $p + p$  at 200 GeV.

## 4.2 Run14 Minimum Bias

An analysis goal of this thesis is to see jet modifications in  $Au + Au$  systems at more peripheral centrality classes, and ultimately see how  $R_I$  changes with these more peripheral classes as well. So, we studied how jet modifications change based on the two-particle correlation method in 5% centrality bins across centralities of 40-90% in the MB data set at 200 GeV.

### 4.2.1 Correlation and Jet Function

In Figure 4.3 and 4.4 we used the centrality class of 40-45% to demonstrate the correlation and jet function, respectively. More plots can certainly be used but it is redundant. Trigger and partner bins are the same as the correlation function in the  $p + p$  system.

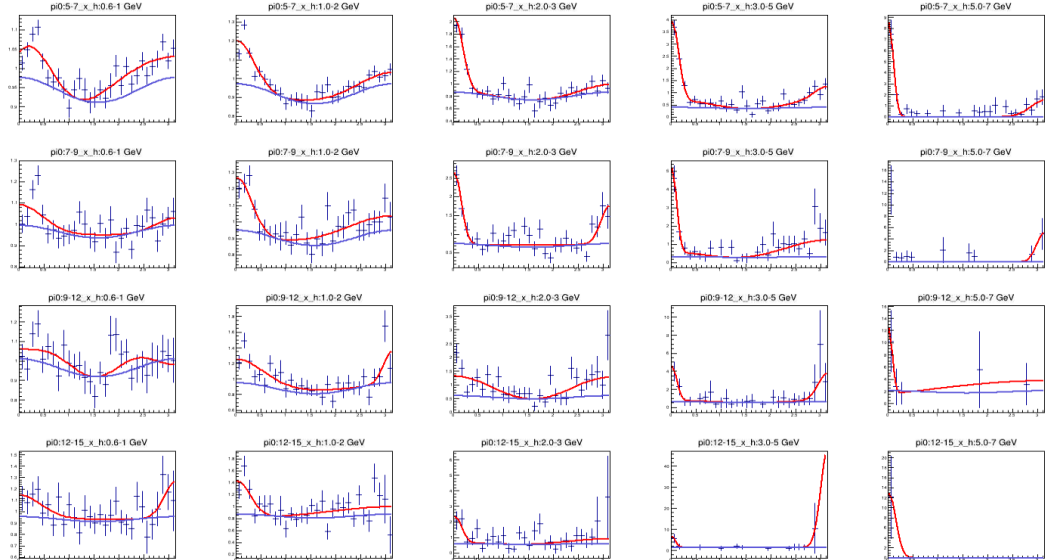


Figure 4.3:  $\pi^0$ -charged hadron correlation function for Run14 MB data set, 40-45% centrality. The red line is the fit to the data and the blue line is the background from the ZYAM method.

In Figure 4.3 there is a problem with the correlations, meaning some subplots have a very poor fit and background at  $\pi/2$  due to noise. Because we see this background in

most plots this may indicate that the matching of same events (foreground) and mixed events (background), which is the detector acceptance correction, is not matching and mixing events properly. Even in the plots that appear to have a good fit such as the trigger  $p_T$  bin of 7-9 GeV/c and partner  $p_T$  bin of 2-3 GeV/c (second row, third column), there is still too much background. We should see the background as  $C(\pi/2) = 0$ . One thing to notice is that there are still peaks at 0 and  $\pi$ , so we still see correlations exclusive to jets, just not with good statistics at hand.

After the background has been removed using the ZYAM method we obtained the jet function for Run14 as seen in Figure 4.4 below.

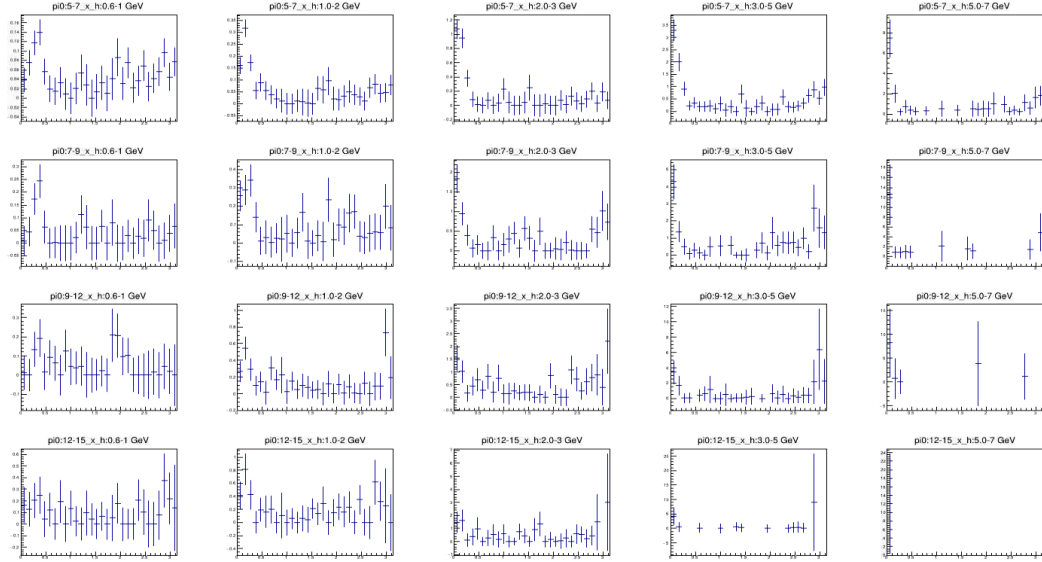


Figure 4.4:  $\pi^0$ -charged hadron jet function of Run14 MB data set, 40-45% centrality. After the background was removed from 4.3, we see a significant amount of noise between zero and  $\pi$ .

Higher centrality classes saw a poor background subtraction as well. Simply put, these results will need to be further studied to determine why, and how, to remove the poor background and produce cleaner correlation and jet functions. One other issue at hand that contributes to the background is the hot tower maps, which will be discussed next.

### 4.2.2 Hot Tower Maps

Hot tower maps are those where dead regions, or an excessive amount of hits occurred in towers of EMCAL. Our development of the framework for this study allows us to view whether the data set has any hot towers by looking at these maps. The hot tower maps produced in Run14, shown in Figure 4.5, indicate that there is an excessive amount of noise in almost half of the entire EMCAL. The plots with red regions are hot towers, which is what we want to remove. In the plots where there is a lot of blue appears as though they are cool towers, but the hot towers are in fact so hot that the scaling causes the normal towers to appear cool. Future work will entail removing these hot towers to allow for a better background, or reduction of noise. This will have a better effect for the correlation and jet functions. The hot tower maps also have an effect on the following double ratio,  $R_I$ . Thus based on our analysis framework, it is clear that the removing systematic effect of the hot towers will be an important step in making the Run14 measurements.

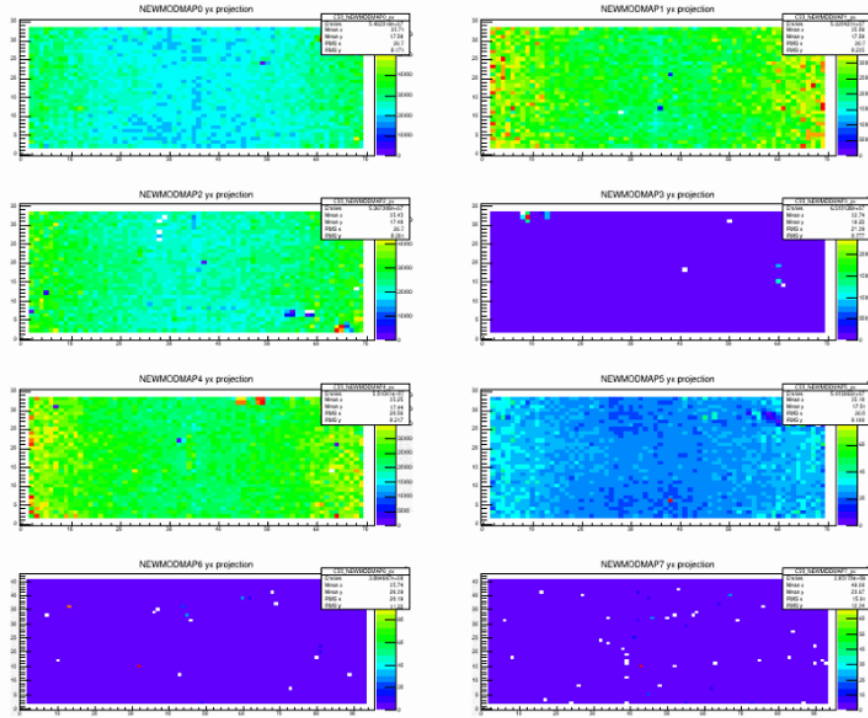


Figure 4.5: The hot tower maps of EMCAL for Run14. Each panel is a sector, and each sector has axes of tower position along the beam line on the x-axis, and the tower height on the y-axis.

#### 4.2.3 Double Ratio ( $R_I$ )

After all correlation and jet function analyses are complete, the double ratio,  $R_I$  is created. The important aspect of this result for the purposes of this thesis is just that it means the framework is developed all the way through the point of making the  $R_I$  vs centrality. For example the last part of this framework, the plotting versus the smaller centrality binning, can be used in the future to assess the possibility of using even smaller centrality binning.

As for the behavior of the data, since the data still does not have all corrections made, interpretations should not be taken seriously. But the behavior already looks somewhat reasonable. In Figure 4.6 we see a near uniform value of  $R_I$  at low  $z_T$ . This tells us that there is no increase in particle yield. What we would anticipate to see at high  $z_T$  is a suppression of  $R_I$  due to our  $p + p$  measurements giving  $R_I$  a

value of 1, and an increase of  $R_I$  at low  $z_T$ . But, we do not see much of a suppression at high  $z_T$ , nor enhancement at low  $z_T$ . This is likely due to the large background noise seen in the CF and JF plots. Once the CF, JF, and hot tower issues are fixed then that should propagate to the  $R_I$  plots. Similar graphs are produced for all other centralities of Run14.

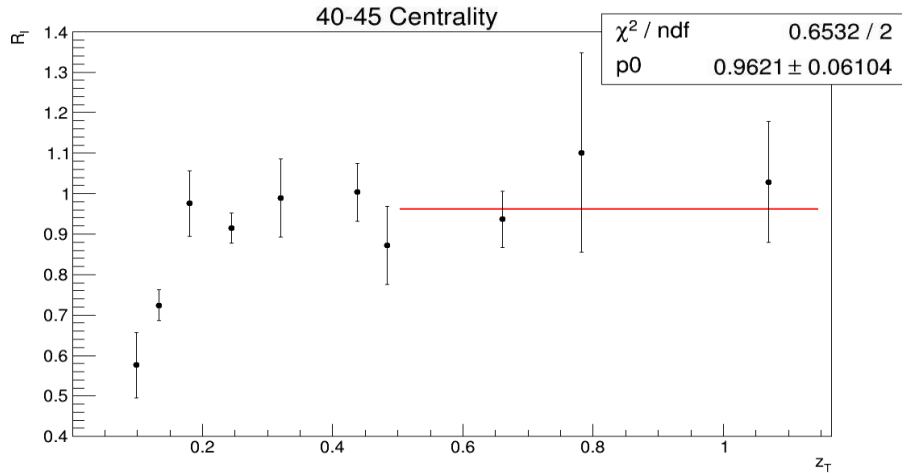


Figure 4.6:  $R_I$  plotted versus  $z_T$  for the 40-45% centrality class, where  $z_T$  is the ratio of the partner-to-trigger  $p_T$ . The constant fit is over the range of  $0.5 < z_T < 1.15$ .

In large systems such as  $Au + Au$ , we expect to see many physical properties change with higher centrality class. For example, particle yield, particle energies, and even the jet energy loss due to the QGP. So, when we plot  $R_I$  versus centrality we anticipate to see  $R_I$  increase towards 1 as we get to more peripheral collisions, although we do not know how fast it will rise or whether it will actually reach or possibly even exceed (due to other nuclear effects) 1. In Figure 4.7 we see an eventual increase in  $R_I$  across centrality class. Because we do not have clean results of our CF and JF plots, we chose to integrate over a different region only for Figure 4.7. That region is from 0 to  $\pi/4$  and then  $3\pi/4$  to  $\pi$ . These regions still contain nearly all the statistics in the jet peaks, which tend to be smaller than half a radian in the particle momentum regions we use. Next, we see how  $R_I$  changes with centrality when we fit  $z_T > 0.2$  and use this new integration range.

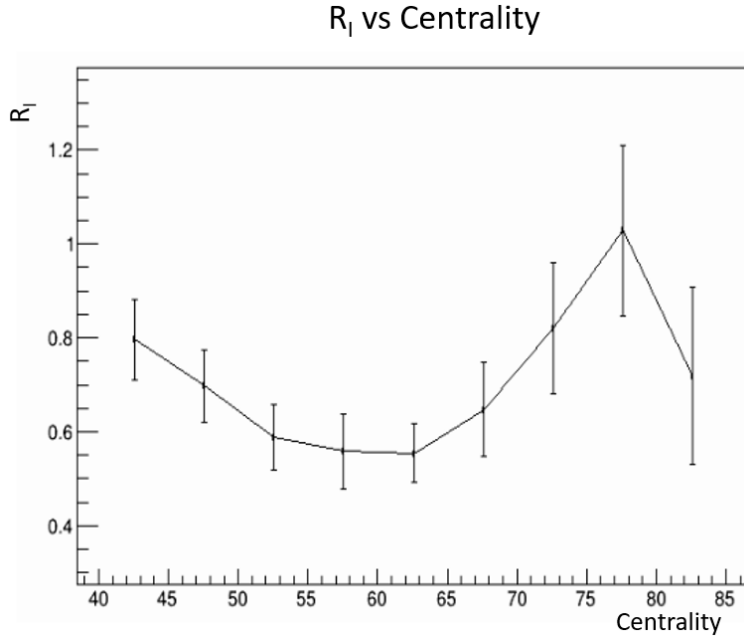


Figure 4.7:  $R_I$  versus centrality classes from 40-90% in 5% bins. This plot is not fully corrected, and therefore is not a final result of any kind.

We cannot trust these values entirely in Figure 4.7. The small increase in the value of  $R_I$  as the collisions become more peripheral in on the right path though. This should happen because the overlap between the  $Au$  nuclei become smaller and smaller, which then restricts the amount of interacting particles, which in turn will not suppress particle production because the QGP is of lesser quantity. This plot simply displays the idea that our initial steps in analysis are in the right direction, with many things to work on.

The Run14 MB data set was then compared with Run 10 to show feasibility and statistical precision of  $R_I$  suppression at high  $z_T$  using  $Cu + Au$  and  $^3He + Au$  systems (see Figure 4.8. The errors in  $Au + Au$  show reasonable error size given we have much more events to use, and as we combine further data sets, such as another trigger called the Electron-RICH-Trigger (ERT) which selects only events with high energy photons, we will reduce such error. The ERT data set is known to contain about 2 to 3 times the statistics of the MB sample analyzed here. The Run16 results shown

in the next section also contain similar numbers of events sampled in both its MB and its ERT trigger datasets. This means that the total statistical increase compared to the previously analyzed Run10 dataset (which was analyzed for similar quantities though not quite the same as the  $R_I$ ) will be a factor of about 5 to 8 more statistics. This implies when all combined the Run14 and Run16 sets should be able to provide detailed information about the behavior of the  $Au + Au$  suppression at very peripheral collision geometries, likely with even an even smaller centrality binning than chosen in this study.

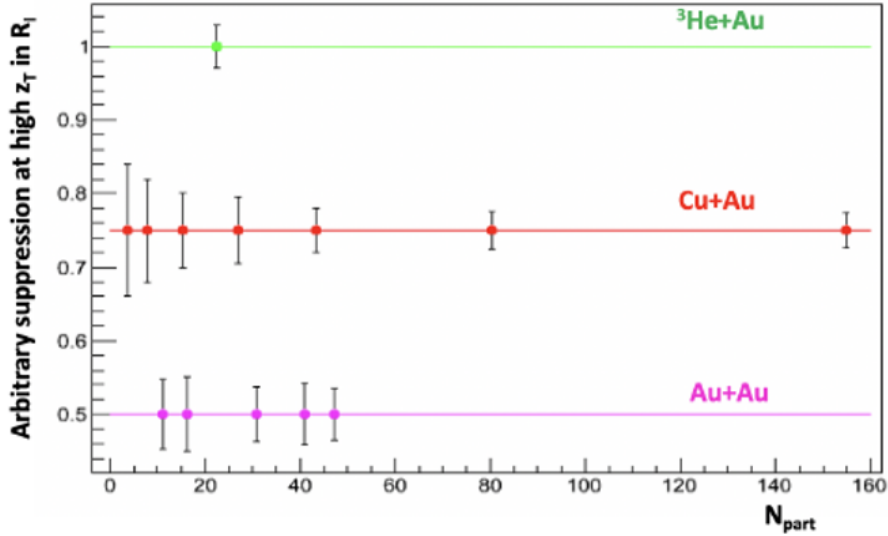


Figure 4.8: A plot of arbitrary  $R_I$  suppression at high  $z_T$  versus the number of participating nuclei ( $N_{part}$ ) for three different systems: Run10  $^3He + Au$  (green) and  $Cu + Au$  (red), and Run14  $Au + Au$  (magenta).

### 4.3 Run16 Minimum Bias

In this section we give results for Run16  $Au + Au$  at 200 GeV usign the MB data set. Run16 had the most statistics available, so this allows the study to have a cross-check to Run14 data.

### 4.3.1 Correlation and Jet Function and Hot Tower Maps

Trigger bins for the  $\pi^0$  and the charged hadrons are the same from Run14. In Figure 4.9 we see a poorer two-particle correlation for all trigger and partner  $p_T$  bins. One part of this is the event mixing, and another due to the hot tower maps, as mentioned for Run14. For future work we will remove the dead/hot towers and fix the event mixing that is causing a large background. The centrality class of 45-50% was used to demonstrate the CF, JF, and  $R_I$  plots.

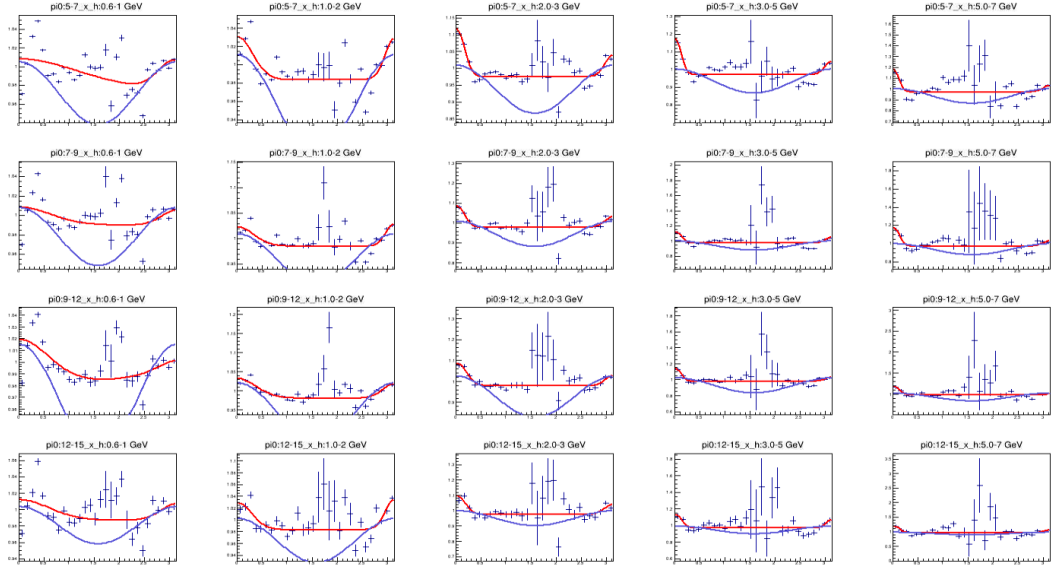


Figure 4.9:  $\pi^0$ -charged hadron correlation function for Run16 MB data set, 45-50% centrality. The red line is the fit to the data and the blue line is the background.

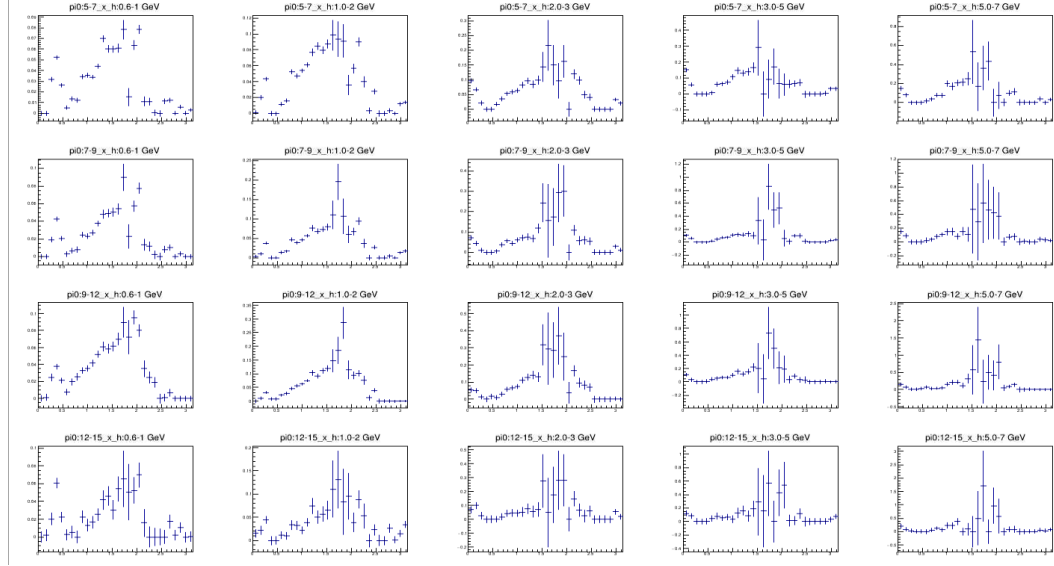


Figure 4.10:  $\pi^0$ -charged hadron jet function of Run16 MB data set, 45-50% centrality. After the background was removed from Figure 4.9, we see a significant amount of noise between zero and  $\pi$ .

The hot tower maps for Run16 have the same description as Run14, and are shown in Figure 4.11. This again is a significant reason why we have poor CF and JF plots, and by fixing them will allow better results.

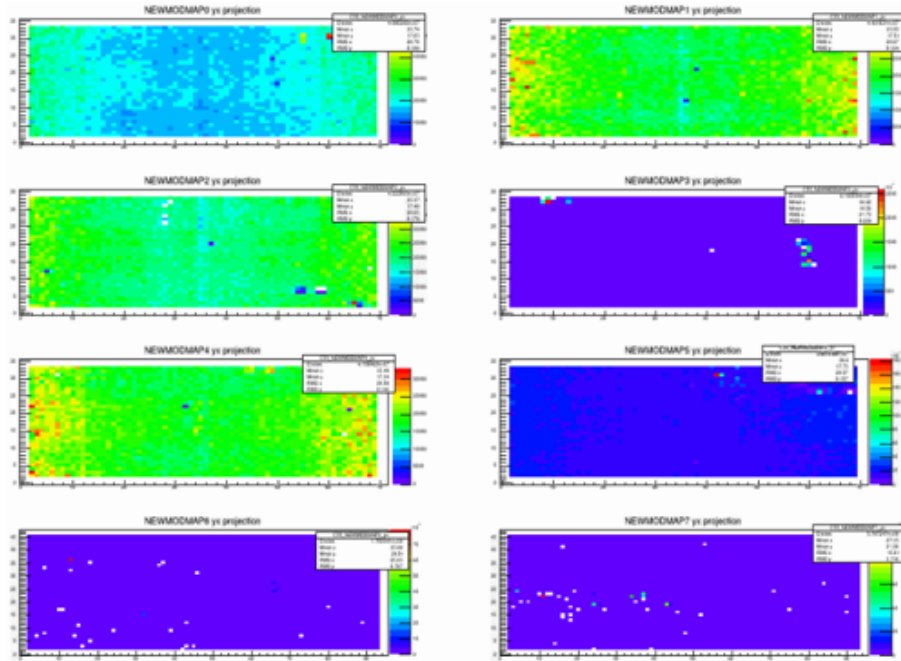


Figure 4.11: The hot tower maps of EMCAL for Run16. Each panel is a sector, and each sector has axes of tower position along the beam line on the x-axis, and the tower height on the y-axis.

### 4.3.2 Double Ratio $R_I$

The double ratio plot seen in Figure 4.12 has a slightly better physical interpretation than Run14's, though we cannot say this is a final result, nor trust all values. We are still demonstrating this as an outcome of our initial framework that analyzes the data sets. Here we see little to no suppression of  $R_I$  at low  $z_T$ , but a possible significant amount at high  $z_T$ . Two data points that do not seem correct are the lowest  $z_T$ 's. Here we expect them to have higher  $R_I$  because there should be a large amount of low  $p_T$  partner particles, thus giving an overall higher particle yield.

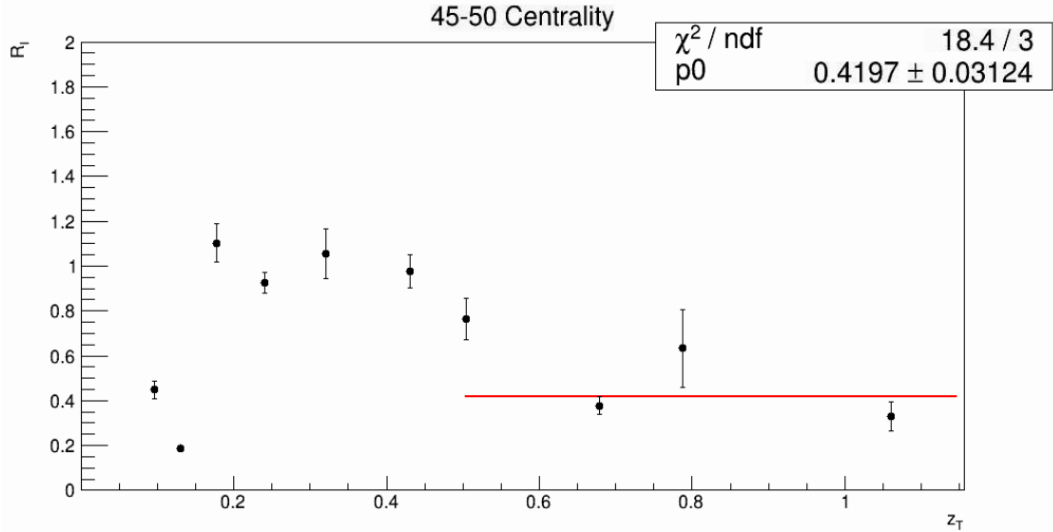


Figure 4.12:  $R_I$  plotted versus  $z_T$  for the 45-50% centrality class, where  $z_T$  is the ratio of the partner-to-trigger  $p_T$ . The constant fit is over the range of  $0.5 < z_T < 1.15$ .

In Figure 4.13 we see a bit more promising result with how  $R_I$  changes with centrality. It is to be mentioned that the integration range that was used to eventually generate this plot was from zero to  $\pi/8$  and likewise for the away-side jet. Also, we used a fit range where  $z_T > 0.5$ . We still cannot trust these values entirely as already explained. One point to make though is we still see a small increase in the value of  $R_I$  as the collisions become more peripheral. This should happen because the overlap between the  $Au$  nuclei become smaller and smaller, which then restricts the amount of interacting particles, which in turn will not suppress particle production because the QGP is of lesser quantity.

The Run16 results shown have not included the ERT data sets, which will add about 2 to 3 times more statistics as well. Again, this means that the increase in statistical precision compared to the Run10 dataset will be a factor of about 5 to 8 more. This implies when all combined the Run14 and Run16 sets should be able to provide detailed information about the behavior of the  $Au + Au$  suppression at very peripheral collision geometries.

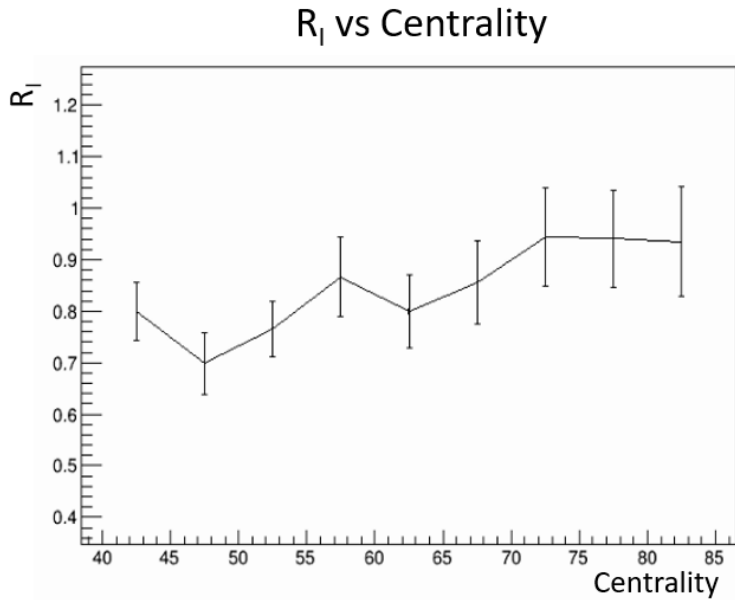


Figure 4.13:  $R_I$  versus centrality classes from 40-90% in 5% bins.

## 5 Part II: Tools and Studies for Relative Calorimeter Calibrations in sPHENIX

In this part of the thesis we discuss work performed in relation to the sPHENIX experiment. This part of the thesis will be focusing on describing the development of calibration tools for three of the subdetector systems that have already been presented in sections 2.4.1 and 2.4.2. Particularly, we have developed a relative calibration technique that can be used to normalize the calibration on a tower by tower basis such that all towers are adjusted to have the same "gain" calibration. The term "relative" refers to the fact that the method is not concerned with whether the calibration is exactly correct itself, and it is assumed that other methods, such as a pi0-mass-based method, can be used to do a further step to verify the accuracy of the absolute overall calibration. This will be further clarified below. Thus the relative calibration is the first step in a chain of techniques that will ultimately produce a complete calibration. In this first relative calibration step, the goal is only to ensure that the calibration is uniform (even if not completely correct) across the thousands of towers in each calorimeter system. Using simulation software packages known as GEANT4 and PYTHIA, we generate close to real world data which is then analyzed. Later we describe the development and demonstration of a simple Monte Carlo to further test and verify such work. These tools are used to determine an estimate of the number of events needed to make the relative calibration uniform across all towers to within a certain relative precision in sPHENIX. The tools are also used to begin the process of eventually developing the full relative calibration and the associated correction factors.

## 5.1 Introductory Information

In the beginning of this section we describe some of the ingredients and background information and then, in Section 6 present the results of several analyses using these ingredients.

## 5.2 Calorimeter Calibration

As described previously, the way both sPHENIX hadronic and electromagnetic calorimeters work is by converting light emitted from incident particles into a voltage pulse. Each tower has a light collecting device, a silicon photomultiplier (siPM) (Hamamatsu S12572) which will perform this conversion of light signal to voltage pulse. An Analog to Digital Converter (ADC) for each siPM will digitize the pulse height or amplitude such that the energy of the particles detected by the tower can be described by the following linear relation

$$E_{tower} = C_{gain,tower} \times N_{ADC,tower} \quad (5.1)$$

The factor  $C_{gain}$  is often called the "gain" in many experimental nuclear and particle physics contexts like this. The calibration factors we are designing the sPHENIX calibration system to find are essentially  $C_{gain}$  for each tower. A rough value of this factor for every tower is already known, based on many factors such as each individual tower's device characteristics, and many previous tests of example situations. However, the final adjustments to  $C_{gain,tower}$  for each of the 27,000 different tower units across the three sPHENIX calorimeter systems can only be made after they are constructed and installed. This is the calibration for which our studies of the relative calibration are aiming to provide. Specifically, the relative calibration aims to find those parts of the adjustments to ensure that  $E_{tower}$  will be the same for the same physical particle detection in each tower, even if the actual value of  $E_{tower}$  is

not necessarily the desired correct energy of the particle. Once the relative energy calibration method that we are aiming to develop is applied, then one overall factor (called the overall energy "Scale") can be used to adjust all tower gain factors to the correct value. In this way we factorize the problem of the calibration into two parts, the relative calibration (different for each tower) and the final absolute scale calibration (common to all towers). The adjustment factors are a chain of corrections according to the equations  $E_{uniform,tower} = C_{adj,tower} \times C_{gain,rough,tower} \times N_{ADC,tower}$ ,  $E_{final} = C_{scale} \times E_{uniform}$  and  $E_{uniform} \equiv E_{uniform,tower}$ .

Our method for developing the relative calibration relies on the idea that over many events, if all towers have the same relative calibration, the energy distributions for all towers measured over those events will have exactly the same functional shape, at least above some minimum energy. This is because these distributions should be determined by the underlying physics of the collisions which is known to be the same over large regions of the, if not the entire, detector acceptance.<sup>3</sup> Conversely, the extent by which the shape differs tower to tower can be used to generate the desired  $C_{adj,tower}$  factors for each tower.

The rough functional shape  $f(E)$  is expected to be exponential at low energy. To an extent this is true, and then our adjustment factor can be derived from an exponential slope factor of each tower's distribution. Using simply the exponential slope itself has been successfully used for this purpose in the PHENIX experiment and other experiments in the past, thus we will sometimes refer to the method as the slope method, although it is expected that the method will need to be developed beyond a simple exponential assumption. Exponential shapes are also relatively simple to deal with since a log-scale linear fitting, or possibly even other direct linear slope

---

<sup>3</sup>The underlying physics must be phi-symmetric averaged over many events because all of the reaction planes transverse angles are sampled uniformly by two overlapping beams. The reason it is expected to be largely symmetric in  $\theta$  and pseudo-rapidity  $\eta$  (the reader is reminded that both  $\eta$ , which is a monotonic function of  $\theta$  denote direction along the beam line) is due to the detector being in the "central rapidity region" [26]

calculation methods, can be employed, which makes it worth studying as a first candidate. Therefore the first step is to find the expected energy distribution in each tower.

### 5.3 HIJING and PYTHIA

In the early stages of an experiment in particle physics it is typical to develop an understanding of what physics is desired to be studied and how to design an experiment to verify theory. One part of this process is called an event generator. An event generator is a computer simulation (typically using Monte Carlo techniques) in which it strives to create events (particle collisions and the aftermath) that are comparable to real data. Some purposes for an event generator in particle physics is to understand what events may occur during an experiment, help optimize and even build detector systems, and help develop strategies for data acquisition. The sPHENIX detectors outlined in this thesis utilize the event generators called PYTHIA and HIJING for calibrations. PYTHIA [27] [28] generates particle-hadron collisions and in heavy-ions it is most often used as a proxy for actual proton-proton collision data. HIJING [29] is a nuclei-nuclei high energy event generator, largely based on PYTHIA which it uses in a way that combines many p+p, n+n, and n+p PYTHIA collisions, together with more sophisticated handling of soft particle production (though it does not include a microscopically-detailed QGP) and many known cold nuclear physics effects. As sPHENIX will need to use both p+p and Au+Au data to calibrate, the tools developed for this thesis were demonstrated over both PYTHIA p+p and HIJING Au+Au samples, however the resulting demonstrations presented in this thesis are exclusively from running over HIJING events, other than the simple monte carlo presented later.

## 5.4 Energy Distributions

After HIJING or PYTHIA has generated events, data in the form of energy and position (among many others that aren't important to this study) is stored. This is similar to the information collected in the real data. Whether real, or PYTHIA, data, our analysis then starts with extracting the energy distributions (see Figure 5.1 for an example) for each tower in each detector subsystem. This is done by creating a unique histogram to store each of the thousands of towers'  $E$  distribution. When integrated over many events, as these distributions will be, the physics must be symmetric across all phi bins at a given pseudorapidity ( $\eta$ ) bin. We also create histograms for each eta bin with the energy distribution integrated over all phi bins (which is what is seen in Figure 5.1). The energy distribution in this plot is from all towers from a single eta bin with a 0 to  $2\pi$  integration. Since the y-axis is a log-scale, it is obviously a very quickly falling energy spectra, but more importantly it is linear on in some regions. This implies the distribution is similar to exponential.

The exponential shape of the spectra (and the ultimate function form for the energy fit used in later sections) is of the form

$$f(x) = Ae^{-p_1x} \quad (5.2)$$

where  $A$  will also be described sometimes as a constant of the form  $e^{p_0}$ ,  $p_1$  is called the slope (the slope of the line when plotted on log-y-scale), and  $x$  is energy in GeV. The reason the energy distribution is approximately an exponential is because in the energy range between about 0.5 to 3 GeV, the physical processes of particle production in heavy-ion collisions, which drives the spectral shape, can be described with a Boltzmann distribution, whose behavior is exponential. The Boltzmann distribution tells us what a system's final state will be based on temperature and energy, two quantities that are understood in heavy-ion collisions. Even in  $p + p$  collisions such

as those that the PYTHIA generator makes, the soft production processes in the low energy regions are still empirically known to be approximately exponential. At higher energies the underlying physical process driving the distribution is "perturbative" QCD processes, and is expected to be of a power law form.

As will be shown in Section 6, we will fit Eq. 5.2 among different ranges in each detector and extract p1. p1 is important to this study as we will be using it to show how the energy distribution changes with  $\eta$  in each detector and ultimately derive the relative calibration factors  $C_{adj,tower}$  from it.

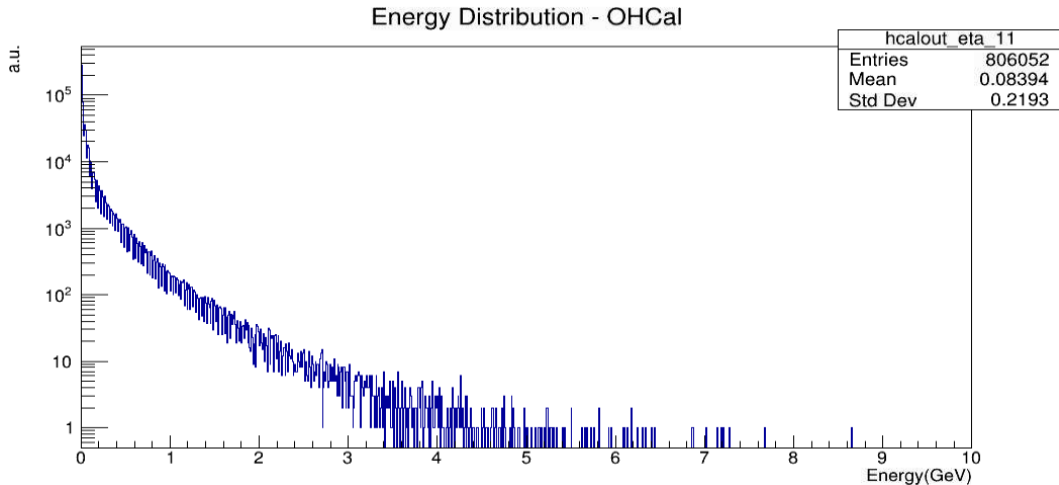


Figure 5.1: An energy distribution for the outer hadronic calorimeter. This histogram is from  $\phi$ -integrated eta bin number 11, which is close to  $\eta=0$  in pseudorapidity.

As shown in Section 6, the fitting process differs detector by detector. The reason being because of sensitivity to energy deposition. For example, the IHCal has the fewest fit ranges because the overall energy collected is low due to it being very thin. Most hadronic showers will only barely start in the IHCal before exiting and continuing the shower, given that there hasn't been enough material to traverse to cause them to fully develop. The lowest energies are not fitted in any detector as well. This is because the lowest energy is the minimum ionizing particle peak, or MIP peak region. When particles enter a medium, and in this case scintillator material, there is a minimum amount of energy needed to produce Cherenkov radiation, but

once the energy is greater than this threshold, the amount of energy loss is small. Because we have a large system, a lot of particles are produced that have at least the minimum amount of energy to make cherenkov radiation. These very low energies may be possible to use as well, but for now we avoid this area since its shape has a different cause compared to the area of the distributions driven by the average particle production which should be the same for all towers. So, we neglect this low energy region in the calibration process as well.

## 5.5 Energy Shifts

We want to ensure that in a controlled Monte Carlo situation that we can extract changes in a calibration. Under the assumption that the energy distribution is purely exponential in shape, means that a ratio termed  $C_{adj,shift} = p1_{noshift}/p1_{shift}$ <sup>4</sup>, gives back a shift itself. An energy shift of the form

$$E' = E \pm const \times E = C_{shift} \times E \quad (5.3)$$

with  $C_{shift} = 1 \pm const$  is used. In Section 6 we will see the results of energy shifts, and discuss the implications of assuming such a distribution.

## 5.6 Monte Carlo Simulation And Alternate Functional Forms

As part of these considerations, we arranged a simple (compared to PYTHIA/HIJING) Monte Carlo simulation as a cross check. The simple Monte Carlo samples a random number generator for energies according to a given generating functional form—at first an exponential with no energy shift. Each energy value sampled is stored in a histogram for a non-shifted value and a shifted value. Various fitting procedures (e.g. function, fit range, etc.) can be then attempted. Besides using an exponential form

---

<sup>4</sup>Here we actually have flipped the ratio in order to show in the Results section that the data shifts according to the shift we give. Otherwise we would have the ratio as  $p1_{shift}/p1_{noshift}$

for a generating function, a function of the form that is commonly used at RHIC is the following

$$f(x) = \frac{a}{(b+x)^c} \quad (5.4)$$

where  $x$  is energy in GeV, and  $a, b$ , and  $c$  are parameters. This function has a nearly exponential shape at low  $x$  but then becomes harder (weighted toward higher energies) with a power law-like tail to high  $x$ .

## 6 Results for Part II: Simple MC Studies, Fitting PYTHIA Distributions, and Estimation of Required Number of Events for Calibration

In this results section we further describe the tools developed and some examples of their use. Most importantly, we use them to estimate the needed statistics for making the desired calibration and begin to study the effects of non-exponential spectral shape. It is very important to determine the distribution because we will perform a relative tower by tower calibration that will be used later to extract correction factors. In all, fit correction factors are simply a function of the fit parameter and an energy shifted fit parameter, which is needed to allow all towers in all detectors to have the same initial gain.

### 6.1 Simple Monte Carlo and Associated Studies

When running the Simple Monte Carlo with Eq. 5.4 and Eq. 6.1, a +5% energy shift and -5% energy shift was included to determine if our analysis code can process correctly the energy distributions as true, or very close to true, exponentials. The non-shifted distributions themselves are not the focus. In all plots of this section we fit the distributions over the range of 0.5 to 1. For now, we choose these regions to fit the general shape we see in the energy distributions of the calorimeters, and not the actual fit ranges discussed e.g. in the later HIJING data studies.

#### 6.1.1 Simple MC: True Exponential Distribution

To verify the calibration method can work in the relatively simplest case of an underlying exponential spectra, we first verify a simple exponential fitting to a case, where for the underlying shape, we use a true exponential function of the form

$$f(x) = A \cdot e^{-9 \cdot x} \quad (6.1)$$

The MC then repeats the same number of trials, events, and ratio of a energy shift of our specifications. The first energy shift tested for this trial *const* in Eq. 5.3 was set to negative 0.05 to denote a negative 5% shift. So, in the following plots we introduce such shifts from Eq. 6.1. In each plot there are two histograms; the blue histogram represents the shifted energy values and the blue solid line is the fit. Likewise for the red colored histogram and its fit.

Given that we generate the data with a true exponential, we expect the average  $C_{adj,shift}$  value to be 0.95. Over five trials of 1,000,000 events, the negative energy shift averaged a  $C_{adj,shift}$  value of  $0.9503 \pm 0.0013$ . What these results reveal is that our assumption of the energy distributions being exponential were correct. So to reiterate the idea goes as follows. If we believe the energy distributions in the calorimeters are exponential and generate a tool that also does the same thing, then we should see with our tool that if an energy shift is provided the distributions should also shift by whatever shift we give. Next we introduce the results for the +5% energy shift.

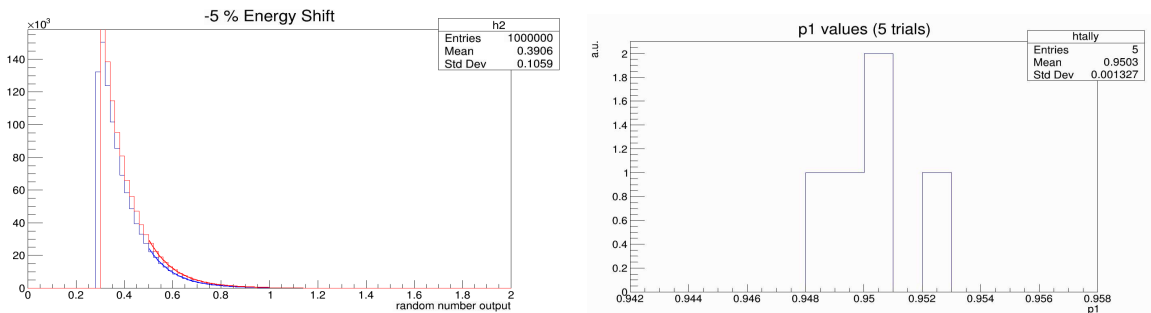


Figure 6.1: Left panel: Monte Carlo output results from Eq. 6.1 is the red data, and the energy shifted results in blue. The x-axis extends to 10, but for a better visual we used a zoomed in image. Right panel: The average  $C_{adj,shift}$  value over 5 trials.

In Figure 6.2 we see the same set up as Figure 6.1, the energy shifted histogram is blue while the non shifted energy is in red. The results show that over the 5 trials the average  $C_{adj,shift}$  value is  $1.0496 \pm 0.0016$ , precisely what we expect given a true

exponential fitting. The statistical error is less than 1 percent. Later we will see if the data from HIJING gives similar results.

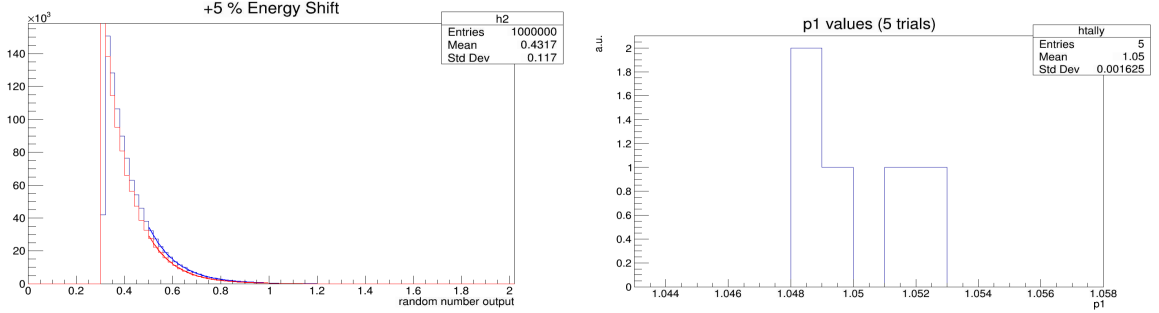


Figure 6.2: Left panel: Monte Carlo output results from Eq. 6.1 is the red data, and the energy shifted results in blue. The x-axis extends to 10, but for a better visual we used a zoomed in image. Right panel: The average  $C_{adj,shift}$  value over the 5 trials.

### 6.1.2 Simple MC: RHIC Distribution

Now we want to generate the energy distributions with Eq.5.4 but still use a exponential fit on the generated histograms. The assumption of an exponential energy fit to the distribution made in the previous section still applies here, but now we want to use this new distribution and determine how well the method can perform. In Eq. 5.4 the parameters  $a$ ,  $b$ , and  $c$  are parameters with fixed values of  $10^8$ , 1.1, and 6, respectively. We loop over 5 trials each with 1,000,000 events, then introduce the same  $\pm 5\%$  energy shift for each trial, checking the ratio  $C_{adj,shift}$ .

We see in Figure 6.3 below using a -5% shift that Eq. 5.4 does generate a well averaged  $C_{adj,shift}$  value compared to that of the true exponential distribution with it being  $0.9691 \pm 0.0010$  over the 5 trials, just not as accurate. This is to not say that the RHIC distribution is wrong though as it still gives good results. Also, these distributions do not reproduce the MIP peak, which in our case does not affect the overall results and implications of the study.

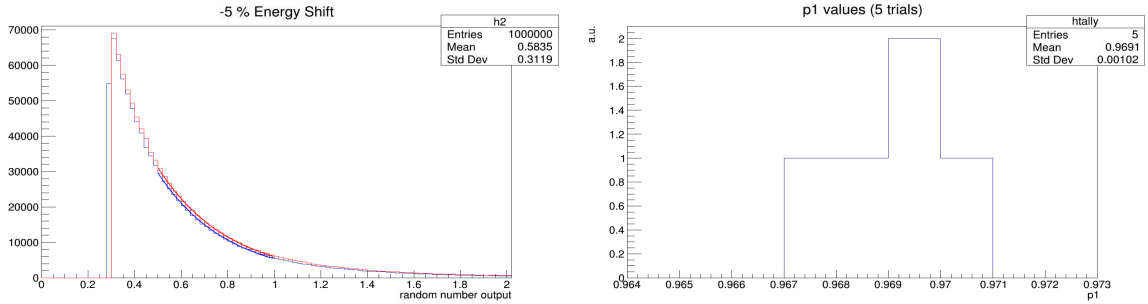


Figure 6.3: Left panel: Monte Carlo output results from Eq. 5.4 is the red data, and the energy shifted results in blue. The x-axis extends to 10, but for a better visual we used a zoomed in image. Right panel: The average  $C_{adj,shift}$  value over the 5 trials of the shifted energy.

In Figure 6.4 we see the results of the +5% energy shift with the RHIC distribution. Over the 5 trials the average  $C_{adj,shift}$  value is  $1.0302 \pm 0.0023$ .

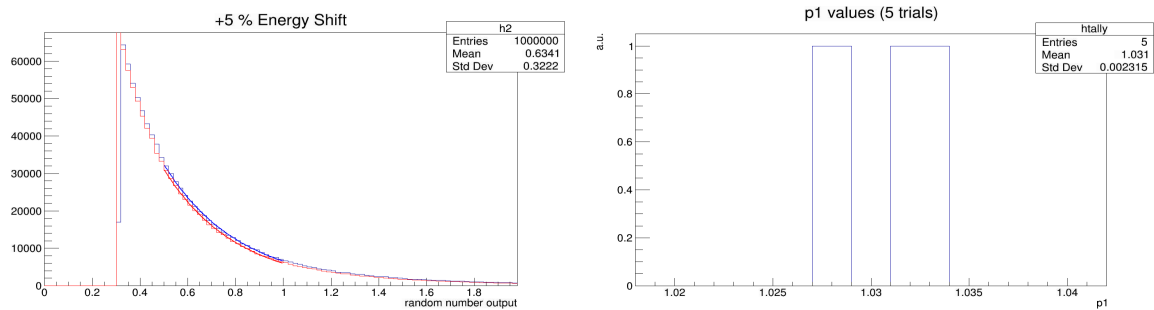


Figure 6.4: Left panel: Monte Carlo output results from Eq. 5.4 is the red data, and the energy shifted results in blue. The x-axis extends to 10, but for a better visual we used a zoomed in image. Right panel: The average  $C_{adj,shift}$  value over the 5 trials.

The RHIC distribution results are clear in that on average it does not generate more accurate  $C_{adj,shift}$  values than the true exponential distribution. Moving forward we will now present data from the HIJING simulation with all three detectors using the idea that the energy distributions are exponential. Data sets part of the first mock data challenge (MDC1) are used where hundreds of thousands events were generated for each detector system.

What we want to know is how many events are needed to give a low relative statistical uncertainty for calibrating the detectors. We are judging the precision

solely on the relative error size of the p1 parameters. This is because the precision of the p1 values is the same as the precision of the adjusted tower based on the equation

$$C_{adj,tower} = p1_{adj,tower}/p1_{true} \quad (6.2)$$

where  $p1_{adj,tower}$  is the p1 value of a tower that needs to be adjusted, and  $p1_{true}$  is the average p1 taken from fitting the combined, integrated histograms of all the towers together. This will give better statistical precision compared to each individual  $p1_{adj,tower}$  value.

Now, applying the methods introduced in Section 5 can now be implemented to the HIJING and PYTHIA data, and compared with the mentioned MC studies. Ideally, we first we must find regions in which our energy distributions appear as exponential, then fit different regions of the distribution, and implement energy shifts. The anticipated outcome is that we see in each detector our  $C_{adj,shift}$  values to reflect a  $\pm 5\%$  shift.

## 6.2 HIJING Studies: IHCal

For the next three sections we turn to analysis of the pseudo-real data from HIJING. We treat the three different calorimeter types in each section the same way, starting in this section with the Inner Hadronic calorimeter (IHCal), going through all aspects of the analysis, demonstrations of the tools, and results for each. For all of these three sections, no "truth" information (perfect as input into the detector simulation) is accessed, we only access detector reconstruction after the GEANT4 detector simulation as if it were real data. Thus, all experimental quantities shown are "reconstructed" by the detectors with detector imperfections. For example *eta* binning corresponds to which geometric *eta* (essentially  $z_{EMC}$ ) position that was hit by the electromagnetic or hadronic shower. The energy distributions for each tower,

or in some cases, integrated over certain areas such as rings of  $\eta$ , are collected for the three calorimeters. We immediately apply the fitting analysis to this data in order to first assess the potential statistical precision of the fits and to study the "data" systematic trends. The IHCAL energy fit ranges were 0.02-0.1 GeV and 0.1-1 GeV for the reason as described in Section 5.4. Also, the IHCAL is very close to the beam line, so it is not as sensitive to higher energy hadronic showers compared to, say, the OHCal that is at a farther distance. Thus for IHCAL at first inspection, only two fit ranges were appropriate. As shown in Figure 6.5, the second fit (teal) starts to miss the data though as energy increases. What may need to happen in future work is use different fit regions, or more of them. So, this is one area where further investigation can be now made with the tools developed.

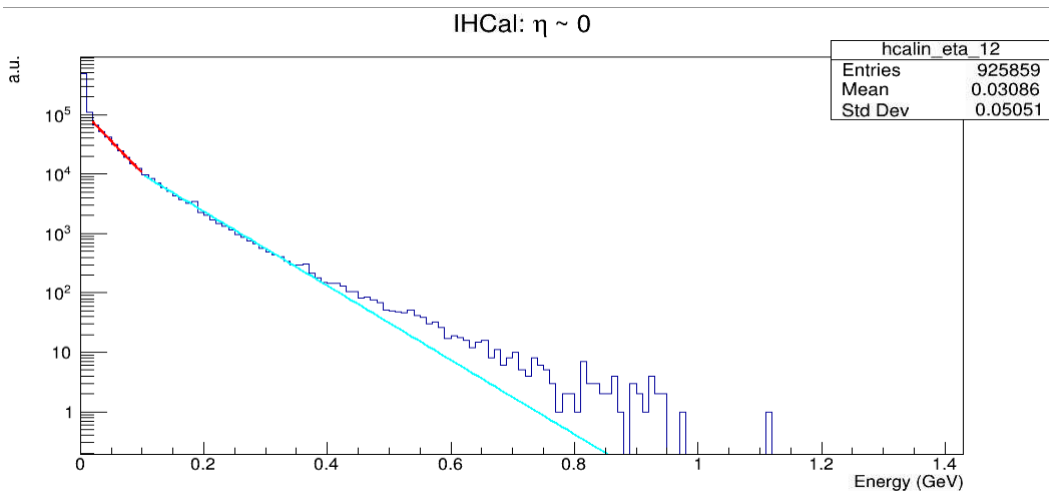


Figure 6.5: Plotted is the energy deposition at approximately  $\eta = 0$ , so directly above the collision vertex (see Figure 1.4). The y-axis is in logarithmic arbitrary units and the x-axis is energy in GeV. The red fit has a range of 0.02-0.1 GeV, and the teal fit from 0.1-1 GeV.

After the energy distribution plots have been fitted with the exponential function Eq. 5.2,  $p_1$  is extracted. We then need to see how  $p_1$  changes with pseudorapidity,  $\eta$ . In Figure 6.6 we first note that the x-axis is plotted from 0 to 23 because of 24 towers in  $\eta$ , which is a bit misleading due to the fact that  $\eta$  actually ranges from -1.1 to 1.1. So, the 0 eta bin corresponds to -1.1 in pseudorapidity and 1.1 to eta bin 23.

The second fit region results are shown using 125,000 events. As noted in a previous footnote, the distribution of the underlying physics should be relatively constant with  $\eta$ , but there can still be some effects that can cause an  $\eta$  dependence, though the left panel of the Figure 6.6 demonstrates (note the offset from the origin of the y-axis) a quite modest relative  $\eta$  dependence of the fit p1 value: an under 10%, smooth variation for most of the *eta*-range reaching 20% at the very end. It is expected that optimization of the method, such as using a more restricted fitting range, can include reducing these relative  $\eta$  dependences (seen in all three calorimeters) even further, and the final strategy would be to expect to use HIJING as the best estimation of this  $\eta$  dependence, and include its expected modulation in the determined  $C_{tower,adj}$  factors. Any even smaller further mismatch between the data and HIJING simulation in this regard could then be fixed by some of the later scale corrections which can better assess the absolute calibration's  $\eta$  dependence.

Shown in the right plot of Figure 6.6 is the relative statistical error of the p1 parameter, which as stated before can be used directly as an estimator of the statistical precision of the desired  $C_{adj,tower}$  factors. We see that the relative error in the right panel of Figure 6.6 is below 1 percent, this tells us that we have constrained the tower by tower gain variations well within the 2 percent limit idealization set by sPHENIX. Since this simulation for the 1 to 2% precision level corresponds to 100,000 to 500,000 Au+Au events based on the number of HIJING events, we can expect that the relative calibration for this can easily be done many times during the year of data-taking ( $\sim$  100 Billion Events), which can allow sPHENIX to monitor the time-dependence of the calibration very closely, likely using only a small fraction of the data taken. The latter is important so that the computing processing time can be reduced compared to having to collect every event taken to do this calibration.

Next, we will discuss the results of the p1 ratio with a  $\pm 5\%$  energy shift.

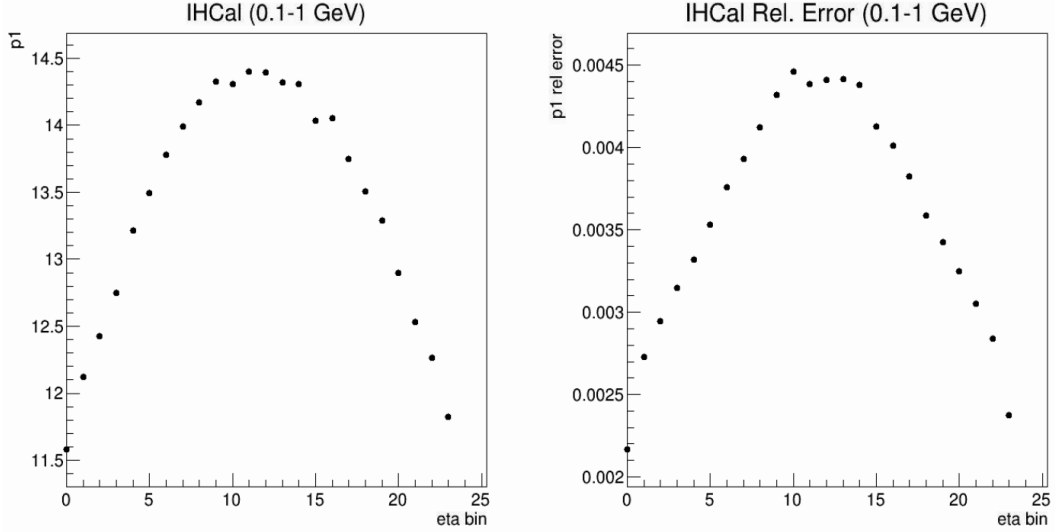


Figure 6.6: Left panel -  $p_1$  versus eta bin plot of the first fitted region in Figure 6.5 (red) of IHCal. Right panel -  $p_1$  relative error versus eta bin.

### 6.2.1 PYTHIA IHCAL Energy Shift

A simple energy shift was applied using Eq. 5.3 for both fit regions. Next we determined  $C_{adj,shift}$ . What we should see in the following figures, in a perfect world, is all the  $p_1$  ratios shifted by plus, or minus 5%. This will tell us if our assumption that the energy distributions are truly exponential. Figure 6.7 shows  $C_{adj,shift}$  of the second region<sup>4</sup>.

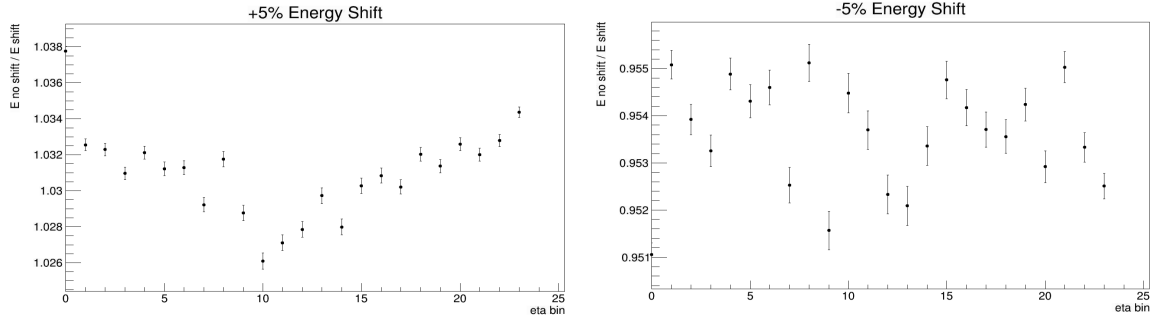


Figure 6.7: Left panel - An energy shift of positive 5% with  $C_{adj,shift}$  versus eta bin. Right panel - An energy shift with a negative 5% shift with the same axes as the left panel.

The left panel of Figure 6.7 shows the positive energy shift of the second fit region.

We see that we do not have a perfect shift of 1.05, so a quick conclusion is that the region we fitted needs to be changed or another optimization of the method related to that the region is not truly exponential. But, this result still shows promise that the fit region is in the right area and the exponential slope method can work reasonably well. The right panel shows a more clear result in that the energy distribution is behaving more exponentially. This is because the average ratio, though it is not the most important to average over the  $C_{adj,shift}$  values, is between 0.953 and 0.954, with errors below 1 percent.

### 6.3 PYTHIA Studies: OHCal

For OHCal and EMcal we collect the energy distributions and start directly with the fitting results. OHCal has fit ranges of 0.05-0.2, 0.2-1, and 1-2 GeV. In Figure 6.8, for example, not all data is fit and the reason for this is poor statistics. This applies to all plots of such as Figure 6.8. The second fit region will be presented in the p1 vs eta plot and in the energy shift results.

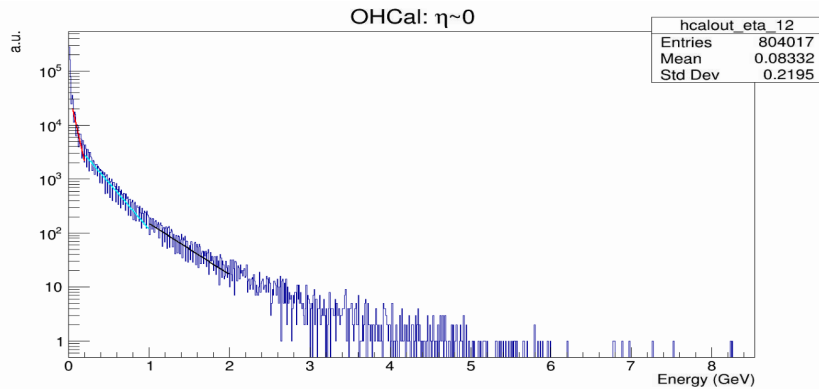


Figure 6.8: Plotted is the energy deposition at approximately  $\eta = 0$ , so directly above the collision vertex. The y-axis is in arbitrary logarithmic units and the x-axis is energy in GeV. The red fit has a range of 0.05-0.2 GeV, the teal fit from 0.2-1 GeV, and the black fit from 1-2 GeV.

In Figure 6.9 below we see the p1 versus eta bin, and p1 relative error versus eta bin. We see almost a constant p1 value from eta bin 4 to eta bin 20 with variations

almost all less than a couple percent. This is not an odd coincidence though. OHCal is the outer most detector system in sPHENIX, so at large radial distances from the beam line, hadronic showering has a very large distribution, thus depositing energy across many sectors in OHCal – this further improves the assumption of a constant  $\eta$  dependence of the spectral shapes, causing histograms among different eta bins to be similar, thus giving similar p1 values after fittings. Before and after this near constant p1 region, p1 values fall off quickly in one bin still showing only a 10 percent difference, most likely due to the low energy particles that have weakly interacted during collisions.

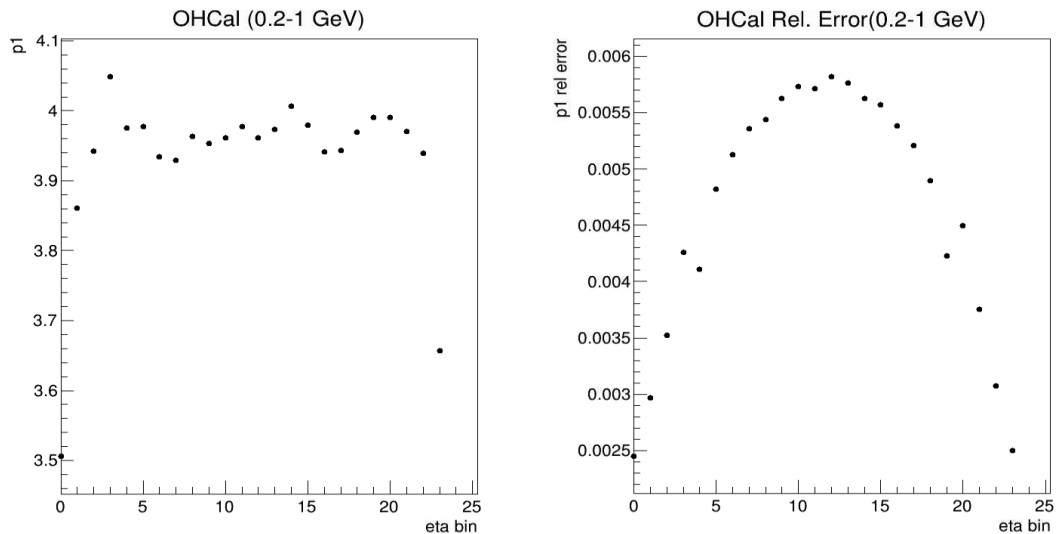


Figure 6.9: Left panel -  $p_1$  versus eta bin plot of the second fitted region in Figure 6.8 (teal). Right panel -  $p_1$  relative error versus eta bin.

With relative error below 1% into what corresponds to 100,000 to 500,000 Au+Au events, we meet again the desired statistical precision set forth by the sPHENIX collaboration and similar conclusions as for the IHcal are apparent, for example making the method possible for many segments of the data in a year and using only a small fraction of the taken data.

Next, we will discuss the results of  $C_{adj,shift}$  with a  $\pm 5\%$  energy shift.

### 6.3.1 PYHIA OHCal Energy Shifts

In this section we show results of OHCal energy shifts and the resulting  $C_{adj,shift}$  values. Figure 6.10 shows the outcome of the energy ratios from the second fit region.

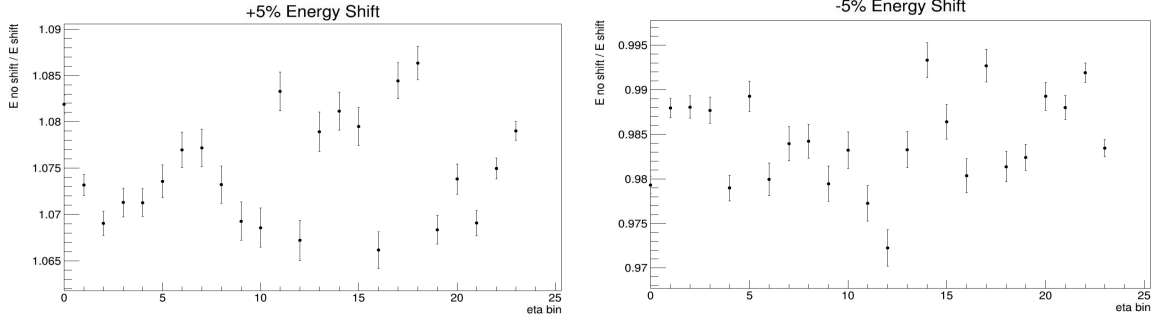


Figure 6.10: Left panel - An energy shift of positive 5% with the p1 ratio's versus eta bin. Right panel - An energy shift with a negative 5% shift with the same axes as the left panel.

The left panel shows a positive energy shift and the resulting  $C_{adj,shift}$  values. The  $C_{adj,shift}$  values are little outside of the region of expectation. By eye, the average is about 1.075, which is of course a little higher than expected but the precision of getting a ratio value in the neighborhood of 1.05 is promising. The right panel is the negative shift and the resulting  $C_{adj,shift}$  values. These values fall much higher than the anticipated 0.95, where there is about an average of just above 0.98. Just like the IHCal results, the same idea applies here where changing the fit region may result in a better outcome, or perhaps using a non-exponential fit.

## 6.4 PYTHIA Study: EMCAL

In this section we outline the EMCAL results in the fitting process of the energy distributions and the energy shift plots. In Figure 6.11 the fit ranges are 0.04-0.11, 0.1-0.4, and 0.4-2 GeV. The second fit region (teal) will be presented in the following results.

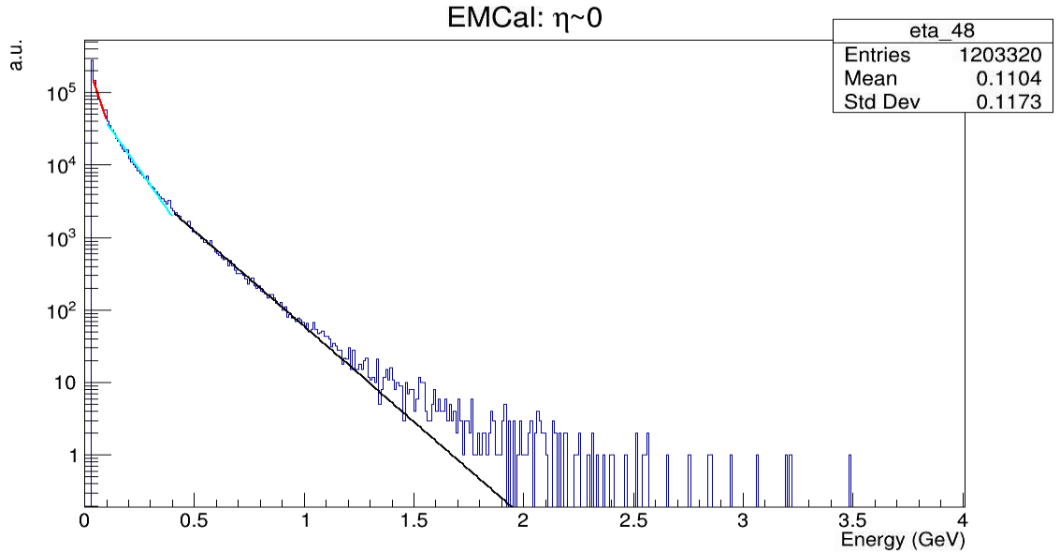


Figure 6.11: Plotted is the energy deposition at approximately  $\eta = 0$ , so directly above the collision vertex. The y-axis is in arbitrary logarithmic units and the x-axis is energy in GeV. The red fit has a range of 0.04-0.1 GeV, the teal fit from 0.1-0.4 GeV, and the black fit from 0.4-2 GeV.

Figure 6.12 below shows the p1 values of the second fit. The left panel does not show a typical distribution that we've seen in the I/OHCal plots. In EMCals, though it is symmetric, there are regions along to the x-axis that begin to form bands, or areas where the value of p1 fluctuates every other eta bin. For example, between eta bin 1 and 14 the odd eta bins have values of p1 that hover around 9.4 and the even eta bins around 9. It is hard to see that in Figure 6.12, but we can see it clearly when zooming with the software package ROOT that is used for this study. The same band forms from eta bin 81 to 95. Then between these regions we still see a similar band structure, but with smaller difference between an upper and lower band. This is likely to be an issue related to the fact that here the statistics are so incredibly high and statistical precision so small and that numerical effects on fitting with such tiny error bars starts showing systematics related to the fitting code. These effects are still under investigation but they don't appear to change any large scale conclusions of the study. This occurrence has also propagated to the energy shift study of EMCal as will be seen in the next section. Right now we are not sure where this error is

emerging from, it is likely as the analysis code works well for IHCAL and OHCal.

The right panel of Figure 6.12 shows an interesting distribution as well. The relative errors form bands. The bands are formed before and after eta bin 50, and it is not clear why it occurs because we don't see such a strong band structure in the left panel, again pointing to numerical systematics possibly deep in the ROOT-standard fitting code. Despite this, again in the just corresponding to 100,000 to 500,00 AuAu events sample size, it's obvious the statistical error falls well below 1 percent level desired by the sPHENIX collaboration.

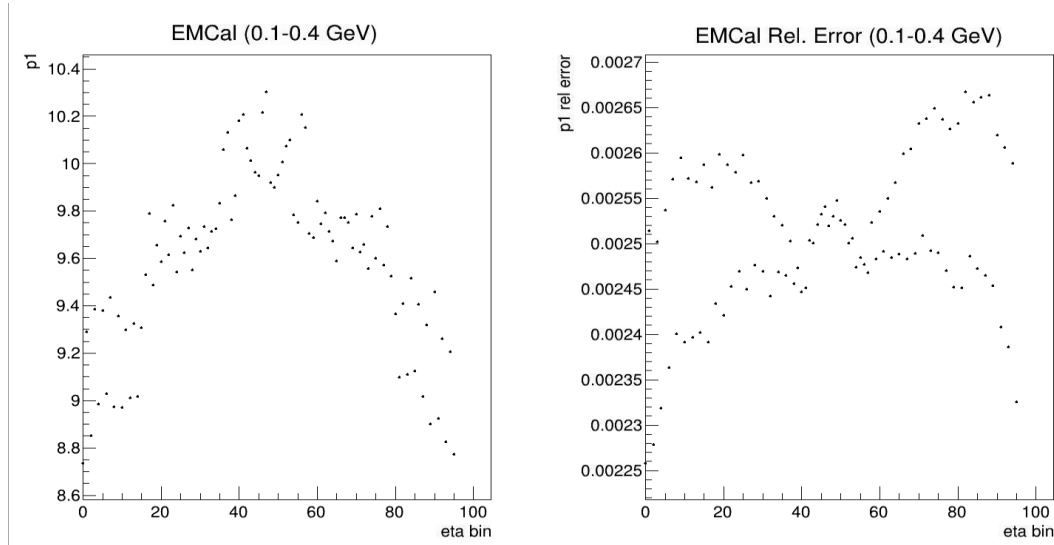


Figure 6.12: Left panel -  $p_T$  versus eta bin plot of the second fitted region in Figure 6.11 (red). Right panel -  $p_T$  relative error versus eta bin.

#### 6.4.1 PYTHIA EMCAL Energy Shift

The energy shift study has yielded similar interesting results for EMCAL as for the other calorimeters. Seen in Figure 6.13 now there are two distinct bands, as described in the previous section, expected to be due to numerical effects due to statistical errors being ultra-small. This will be investigated in future work in both the positive and negative energy shift. In the left panel it appears that one band shifts nearly uniformly at about 1.04. This sign is good, it tells us the fit region responded

well to the shift. But nothing has indicated as to why this does not happen to the lower band, and why it looks like there are small clusters of eta bins that do not respond to the energy shift. The right panel has a very similar pattern. Note that all error bars in Figure 6.13 are smaller than the data points themselves. The upper band appears to have been unaffected by the energy shift while the lower band shifted by negative 5 percent, while pockets of eta bins respond to the shift and others do not. Our expectation, however, is that the  $\pm 5\%$  shift put into the data is indeed affecting both bands but the numerical effects, in both cases, are counter-shifting the bands. Judging by the average shift of both bands and assuming a similar behavior as for the other two calorimeters, it appears that the EMCal over the fit ranges chosen could be shifting less than the input amount, and thus the fit ranges or functional forms need further optimization and development using the simple Monte Carlo, as in the case of other calorimeters.

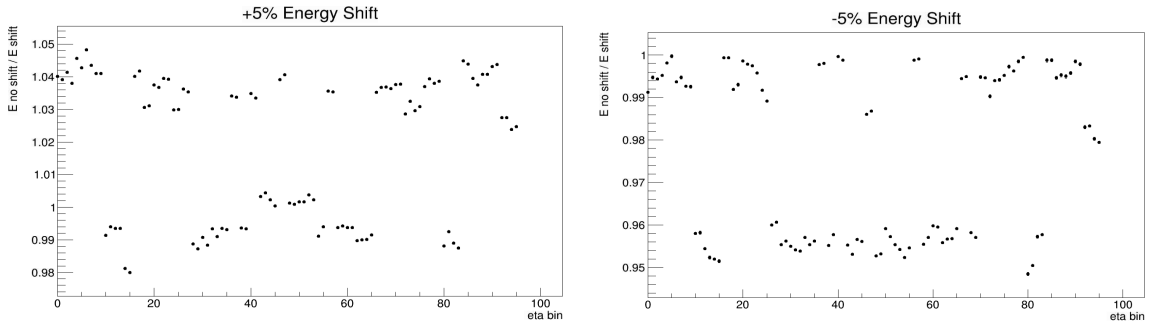


Figure 6.13: Left panel - An energy shift of positive 5% with the p1 ratio's versus eta bin. Right panel - an energy shift with a negative 5% shift with the same axes as the left panel.

## 6.5 Discussion

In this sPHENIX study we have described the tools developed to make the sPHENIX relative calibration with the tower slope techniques. It has been demonstrated that the tools are ready to all determination of the optimization of the methods, including, for example, which regions in the energy distributions appear to behave as true

exponentials. The simple Monte Carlo study yielded promising results as it showed that  $C_{adj,shift}$  corresponded to the shift we gave it. This was not always quite the case for the HIJING studies, though still being promising. Perhaps at the lowest energy, not including the MIP peak, that a Gaussian distribution is best to describe the data, and the rest of the distribution needs to be fitted with an exponential, or many exponentials among smaller regions. Furthermore, it may mean we use a non-exponential fit to the data. Future work will determine the best way forward, and through the work of the thesis the toolset for doing so is developed.

## 7 Summary & Outlook

This thesis was devised for several reasons. First, we wanted to develop a framework that was capable of reproducing the correlation and jet functions that are common among this field of study using  $Au + Au$  collisions at  $\sqrt{s_{NN}} = 200$  GeV with the largest data sets PHENIX had to offer. Run14 MB and Run16 MB had the highest statistics available which allowed us to determine if our framework had statistical feasibility. Also, using the highest statistics available, we wanted to use finer centrality binning to see the jet modifications more and more peripheral collisions take on because of the QGP. In this study we were able to use our developed framework to uncover several issues such as background noise that will need addressed. Future work will include using the hot tower map information collected, and using the Run14 and Run16 ERT data sets. This will add about six times more statistics in this study, which should substantially improve the statistical precision.

The second project of the thesis was developing a framework for detector calibrations of sPHENIXs calorimeters (IHCAL, OHCal, and EMCAL),with the ultimate goal of making a complete, tower-by-tower, relative calibration. The first steps in this calibration was to collect the tower-by-tower energy distributions and fit them to eventually derive a correction factor for the gain seen in all detectors. In addition to this we wanted to determine the number of statistics required for constraining the tower-by-tower gain variations sufficiently. Before we started on this though we developed a Monte Carlo simulation to help better understand a few things. First, we assumed that the energy distribution in the calorimeters was an exponential function, so we created energy distributions from a true exponential and a exponential that is common to the RHIC community. The goal of creating this simulation was to then add an energy shift and ratio the fit value with the shifted energy fit value. The ratio should render whichever shifted value we give, and in our case it was  $\pm 5\%$ . The Monte

Carlo results were very promising in that best distribution was the true exponential. On average the  $\pm 5\%$  shift gave  $1.049 \pm 0.0016$  and  $0.9503 \pm 0.0013$ , respectively. Our results showed that the fit ranges chosen in the calorimeter energy distributions were not exactly exponential in shape. We did not see ratios that exactly reflected the given input shifts. The first change that can be made then is changing the fit regions. We've discussed in the sPHENIX sections the reasons for perhaps different distributions such as the MIP peak at very low energies, and the QCD power law at very high energies. By changing the regions to fit smaller regions it may be beneficial for the ratios. Once we are satisfied with the results we then will go on to produce an overall relative calibration for each detector.

## References

- [1] *Standard Model*. URL: [https://en.wikipedia.org/wiki/Standard\\_Model](https://en.wikipedia.org/wiki/Standard_Model).
- [2] David Griffiths. *Introduction to Elementary Particles*. Wiley-VCH Verlag GmbH & Co. KGaA, 2008.
- [3] *RHIC*. URL: <https://www.bnl.gov/rhic/physics.asp>.
- [4] Miller, Michael L. and Reygers, Klaus and Sanders, Stephen J. and Steinberg, Peter. “Glauber Modeling in High-Energy Nuclear Collisions”. In: *Annual Review of Nuclear and Particle Science* 57.1 (2007), pp. 205–243. DOI: [10.1146/annurev.nucl.57.090506.123020](https://doi.org/10.1146/annurev.nucl.57.090506.123020).
- [5] Ta-pei Cheng. *A College Course on Relativity and Cosmology*. Oxford University Press, 2015. ISBN: 9780199693412.
- [6] *Reaction Plane*. URL: <https://phenix-intra.sdcc.bnl.gov/www/run/drawing/index.html#RPcartoon>.
- [7] Michael L. Miller et al. “Glauber Modeling in High-Energy Nuclear Collisions”. In: *Annual Review of Nuclear and Particle Science* 57.1 (2007), pp. 205–243. DOI: [10.1146/annurev.nucl.57.090506.123020](https://doi.org/10.1146/annurev.nucl.57.090506.123020). URL: <https://doi.org/10.1146/annurev.nucl.57.090506.123020>.
- [8] M. Connors, C. Nattrass, R. Reed, and S. Salur. “Jet measurements in heavy ion physics”. In: *Reviews of Modern Physics* 90 (2018), p. 025005. DOI: [10.1103/RevModPhys.90.025005](https://doi.org/10.1103/RevModPhys.90.025005).
- [9] J. Adams et al. Star Collaboration. “Experimental and theoretical challenges in the search for the quark-gluon plasma: The STAR Collaboration’s critical assessment of the evidence from RHIC collisions”. In: *Nuclear Physics A* 757.1-2 (2005), pp. 102–183. DOI: <https://doi.org/10.1016/j.nuclphysa.2005.03.085>.

- [10] *RHIC Complex*. URL: <https://www.flickr.com/photos/brookhavenlab/%207979381212/in/album-72157613690851651/>, .
- [11] sPHENIX Collaboration. *sPHENIX Technical Design Report*. URL: <https://wiki.bnl.gov/sPHENIX/index.php/TDR>.
- [12] *Run16 Configuration Diagram*. URL: <https://www.phenix.bnl.gov/experiment/auxiliary.html>.
- [13] Adcox, K. et al. “PHENIX detector overview”. In: *Nuclear Instruments and Methods in Physics Research Section A: Accelerators, Spectrometers, Detectors and Associated Equipment* 499.2-2 (2003), pp. 469–479. DOI: [10.1016/S0168-9002\(02\)01950-2](https://doi.org/10.1016/S0168-9002(02)01950-2).
- [14] T. Nakamura. *Introduction to PHENIX Beam Beam Counter (BBC)*. URL: <https://zenodo.org/record/4007995#.YPmGMaYpBE4>.
- [15] M. Chiu. *PHENIX focus; Zero Degree Calorimeter*. DOI: [10.5281/zenodo.4008646](https://doi.org/10.5281/zenodo.4008646). URL: <https://zenodo.org/record/4008646#.YPmKnqYpBE4>.
- [16] S. Milov. “Centrality determination using BBC in  $Au + Au$  and  $Cu + Cu$  collisions at  $\sqrt{s_{NN}}=200\text{GeV}$ ”. In: *PHENIX internal Analysis Note 461* (2005). URL: [https://phenix-intra.sdcc.bnl.gov/phenix/WWW/p/info/an/461/centrality\\_note.pdf](https://phenix-intra.sdcc.bnl.gov/phenix/WWW/p/info/an/461/centrality_note.pdf).
- [17] Adcox, K. et al. “PHENIX central arm tracking detectors”. In: *Nuclear Instruments and Methods in Physics Research Section A: Accelerators, Spectrometers, Detectors and Associated Equipment* 499.2-3 (2003), pp. 489–507. DOI: [https://doi.org/10.1016/S0168-9002\(02\)01952-6](https://doi.org/10.1016/S0168-9002(02)01952-6).
- [18] M. Potekhin. *A selection of photographs of the installation of the PHENIX RICH (East Section)*. DOI: [10.5281/zenodo.4009856](https://doi.org/10.5281/zenodo.4009856). URL: <https://zenodo.org/record/4009856#.YPmcvKYpBE4>.

- [19] L. Aphecetche et al. “The Relativistic Heavy Ion Collider Project: RHIC and its Detectors.” In: *Nuclear Instruments and Methods in Physics Research Section A: Accelerators, Spectrometers, Detectors and Associated Equipment* 499.2-3 (2003), pp. 521–536. DOI: [https://doi.org/10.1016/S0168-9002\(02\)01954-X](https://doi.org/10.1016/S0168-9002(02)01954-X).
- [20] G. Roland. “The sPHENIX experiment at RHIC”. In: 2019.
- [21] sPHENIX Collaboration. *sPHENIX Conceptual Design Report*. URL: <https://wiki.bnl.gov/sPHENIX/index.php/CDR>.
- [22] A. Pun. “Measurements of Di-Jet  $\pi^0 - h^\pm$  Correlations in Light-Heavy Ion Collisions at RHIC-PHENIX”. PhD thesis. Ohio University, 2019.
- [23] B. Xia. “ $\pi^0 - h^\pm$  Jet Correlations in  $d + Au$  Collisions at  $\sqrt{s_{NN}} = 200$  GeV”. PhD thesis. Ohio University, 2014.
- [24] T. Todoroki. “Measurements of Two-Particle Correlations with respect to Higher-Order Event Planes in  $\sqrt{s_{NN}} = 200$  GeV  $Au + Au$  Collisions at RHIC-PHENIX”. PhD thesis. University of Tsukuba, 2014.
- [25] A. Sickles, M.P. McCumber, and A. Adare. “Extraction of correlated jet pair signals in relativistic heavy ion collisions”. In: *Physical Review C* 81.1 (2010), p. 014908. DOI: [10.1103/PhysRevC.81.014908](https://doi.org/10.1103/PhysRevC.81.014908).
- [26] J. D. Bjorken. “Highly Relativistic Nucleus-Nucleus Collisions: The Central Rapidity Region”. In: *Phys. Rev. D* 27 (1983), pp. 140–151. DOI: [10.1103/PhysRevD.27.140](https://doi.org/10.1103/PhysRevD.27.140).
- [27] Torbjörn Sjöstrand, Stephen Mrenna, and Peter Skands. “PYTHIA 6.4 physics and manual”. In: *Journal of High Energy Physics* 2006.05 (May 2006), pp. 026–026. ISSN: 1029-8479. DOI: [10.1088/1126-6708/2006/05/026](https://doi.org/10.1088/1126-6708/2006/05/026). URL: <http://dx.doi.org/10.1088/1126-6708/2006/05/026>.

- [28] Torbjörn Sjöstrand et al. “An introduction to PYTHIA 8.2”. In: *Computer Physics Communications* 191 (June 2015), pp. 159–177. ISSN: 0010-4655. DOI: 10.1016/j.cpc.2015.01.024. URL: <http://dx.doi.org/10.1016/j.cpc.2015.01.024>.
- [29] Miklos Gyulassy and Xin-Nian Wang. “HIJING 1.0: A Monte Carlo program for parton and particle production in high energy hadronic and nuclear collisions”. In: *Computer Physics Communications* 83.2-3 (Dec. 1994), pp. 307–331. ISSN: 0010-4655. DOI: 10.1016/0010-4655(94)90057-4. URL: [http://dx.doi.org/10.1016/0010-4655\(94\)90057-4](http://dx.doi.org/10.1016/0010-4655(94)90057-4).